

NUMERICAL STUDIES OF THE ELECTRONIC PROPERTIES OF LOW
DIMENSIONAL SEMICONDUCTOR HETEROSTRUCTURES

A THESIS SUBMITTED TO
THE GRADUATE SCHOOL OF NATURAL AND APPLIED SCIENCES
OF
MIDDLE EAST TECHNICAL UNIVERSITY

BY

BORA DİKMEN

IN PARTIAL FULFILLMENT OF THE REQUIREMENTS

FOR

THE DEGREE OF DOCTOR OF PHILOSOPHY

IN

PHYSICS

SEPTEMBER 2004

Approval of the Graduate School of Natural and Applied Sciences.

Prof. Dr. Canan Özgen
Director

I certify that this thesis satisfies all the requirements as a thesis for the degree of Doctor of Philosophy.

Prof. Dr. Sinan Bilikmen
Head of Department

This is to certify that we have read this thesis and that in our opinion it is fully adequate, in scope and quality, as a thesis for the degree of Doctor of Philosophy.

Prof. Dr. Mehmet Tomak
Supervisor

Examining Committee Members

Prof. Dr. Cevdet Tezcan (BAŞKENT UNV)

Prof. Dr. Mehmet Tomak (METU, PHYS)

Prof. Dr. Kemal Leblebicioğlu (METU, EE)

Prof. Dr. Çiğdem Erçelebi (METU, PHYS)

Dr. Sadi Turgut (METU, PHYS)

“I hereby declare that all information in this document has been obtained and presented in accordance with academic rules and ethical conduct. I also declare that, as required by these rules and conduct, I have fully cited and referenced all material and results that are not original to this work.”

Name, Lastname : Bora DİKMEN

Signature :

ABSTRACT

NUMERICAL STUDIES OF THE ELECTRONIC PROPERTIES OF LOW DIMENSIONAL SEMICONDUCTOR HETEROSTRUCTURES

DİKMEN, Bora

Ph.D., Department of Physics

Supervisor: Prof. Dr. Mehmet Tomak

September 2004, 86 pages.

An efficient numerical method for solving Schrödinger's and Poisson's equations using a basis set of cubic B -splines is investigated. The method is applied to find both the wave functions and the corresponding eigenenergies of low-dimensional semiconductor structures. The computational efficiency of the method is explicitly shown by the multiresolution analysis, non-uniform grid construction and imposed boundary conditions by applying it to well-known single electron potentials. The method compares well with the results of analytical solutions and of the finite difference method.

Keywords: Basis set, B -splines, low-dimensional structures, multiresolution analysis, electronic structure.

ÖZ

DÜŞÜK BOYUTLU YARIİLETKEN HETEROYAPILARININ SAYISAL
OLARAK ÇALIŞILMASI

DİKMEN, Bora

Doktora, Fizik Bölümü

Tez Yöneticisi: Prof. Dr. Mehmet Tomak

Eylül 2004, 86 sayfa.

Poisson ve Schrödinger denklemlerini çözmek için temel fonksiyon takımı kübik B -spline'ları olan etkili sayısal bir metod incelenmektedir. Bu metod düşük boyutlu yarıiletken yapıların elektron dalga fonksiyonlarını ve öz enerjilerini bulmak için uygulanmıştır. Metodun hesap verimliliği, iyi bilinen tek elektron potansiyellerine çok çözünürlüklü analiz, tekdüze olmayan ızgara yapısı kurulumu ve uyarlanmış sınır koşulları ile ayrıca gösterilmiştir. Metod, analitik çözümler ve sonlu fark methodu ile uyumlu sonuçlar vermiştir.

Anahtar Kelimeler: Temel fonksiyon takımı, kübik B -spline, düşük boyutlu yapılar, çok çözünürlüklü analiz, elektronik yapı.

EŐİM ELÇİN

ve

KIZIM GİZEM'E

ACKNOWLEDGMENTS

I would like to thank my supervisor Prof. Dr. Mehmet Tomak for his support, encouragement, and guidance, for the trust and freedom he gave me during my graduate work.

I also want to thank to my jury members and especially to Prof. Çiğdem Ergelebi for her careful reading and corrections on my thesis.

My special thanks go to Prof. Kemal Leblebicioğlu for his useful discussion and guidance on wavelet analysis.

TABLE OF CONTENTS

ABSTRACT	iv
ÖZ	v
DEDICATION	vi
ACKNOWLEDGMENTS	vi
TABLE OF CONTENTS	viii
LIST OF TABLES	xi
LIST OF FIGURES	xiv
1 INTRODUCTION	1
2 LOW-DIMENSIONAL SEMICONDUCTOR STRUCTURES	6
2.1 Introduction	6
2.2 Modulation Doping	8
2.3 Wavefunction Engineering	9
2.4 Possible Potential Profiles: Model Problems	10
2.4.1 The 1-D Harmonic Oscillator	10
2.4.2 The Attractive δ Potential	10
2.4.3 The 1-D Quantum Box	12
2.4.4 The 1-D Triangular Quantum Well	12
2.4.5 The Symmetric Double Rectangular Quantum Well	13
2.4.6 The Asymmetric Double Rectangular Quantum Well	14
2.4.7 The Double Quantum Well with Softened Coulomb Attraction	14
2.4.8 The Modulation Doped Heterojunction	16

	2.4.8.1	Self Consistent Calculations	17
	2.4.9	Two-Dimensional Single Electron Potentials . . .	22
	2.4.9.1	The 2-D Harmonic Oscillator	22
	2.4.9.2	The 2-D Quantum Box	23
	2.4.10	Three-Dimensional Single Electron Potentials . .	23
	2.4.10.1	The 3-D Harmonic Oscillator	23
	2.4.10.2	The 3-D Quantum Box	24
3		THE METHOD	25
	3.1	Solution of One-Dimensional Schrödinger Equation	25
	3.2	The Multiresolution Analysis Using Cubic <i>B</i> -Spline Wavelets	29
	3.3	Construction of Non-Uniform Grid <i>B</i> -Splines	31
	3.4	Construction of <i>B</i> -Splines Satisfying Arbitrary Boundary Conditions	31
	3.5	Realization of the Self-Consistent Loop	33
	3.5.1	The Details of the Self Consistent Loop	34
	3.6	The Finite Difference Method	36
	3.7	Solution of the Two-Dimensional Schrödinger Equation . .	37
	3.8	Solution of the Three-Dimensional Schrödinger Equation .	38
4		THE RESULTS	42
	4.1	The Effect of <i>B</i> -Spline Order on the Results	42
	4.2	The 1-D Harmonic Oscillator	43
	4.3	The 1-D Attractive δ Function Potential	43
	4.4	The 1-D Quantum Box	46
	4.4.1	The 1-D Quantum Box Satisfying the Imposed Boundary Conditions	47
	4.5	The 1-D Triangular Quantum Well	48
	4.5.1	The 1-D Triangular Quantum Well Satisfying the Imposed Boundary Conditions	49
	4.6	The 1-D Symmetric Double Rectangular Quantum Well (SDRQW)	50
	4.6.1	The Multiresolution Analysis	50
	4.6.2	The Non-Uniform Grid <i>B</i> -Splines	52

4.6.3	A More Compact Representation: Non-Uniform Grid B -Splines Satisfying the Imposed Boundary Conditions	53
4.6.4	A Comparison with the FDM	56
4.7	The Asymmetric Double Rectangular Quantum Well (ADRQW)	58
4.8	The Double Quantum Well with Softened Coulomb Attraction	59
4.8.1	Non-Uniform Grid Treatment of the Double Quantum Well with Softened Coulomb Attraction	59
4.9	Self-Consistent Calculations	61
4.10	Two-Dimensional Case	63
4.10.1	The 2-D Harmonic Oscillator	64
4.10.2	The 2-D Quantum Box	64
4.11	Three-Dimensional Case	66
4.11.1	The 3-D Harmonic Oscillator	67
4.11.2	The 3-D Quantum Box (Finite Quantum Wire)	68
4.11.3	The Finite Quantum Wire with Attractive Impurity	69
5	CONCLUSION	73
	REFERENCES	79
	VITA	86

LIST OF TABLES

2.1	The lowest five eigenenergies of the 1-D triangular quantum well confining potential for $k_x = 1$ defined in Eq. (2.10).	13
2.2	The lowest six exact eigenenergies of the double well potential with softened Coulomb attraction given in Eq. (2.13) for $a = 0.1$	15
3.1	List of the parameters in self consistent loop.	35
3.2	The grid ordering of 2-D mesh given in Fig. 3.5 and Fig. 3.6. The columns and rows in the tables correspond to N_x and N_y basis functions in x and y directions respectively.	38
4.1	The five lowest eigenenergies (E_0 - E_4) of the 1-D harmonic oscillator with $k_x = 1$. In each case $N = 30$ basis functions are used and splines are expanded between $x = -10$ and $x = 10$	43
4.2	The bound state energy level of single $-10\delta(x)$ potential described in Eq. (2.7) for different ϵ values.	44
4.3	The bound state energy level of single $-10\delta(x)$ potential described in Eq. (4.1) for a non-uniform mesh. The basis functions are expanded in the region $x \in [-1, 1]$ and four of the knots are taken closely at the vicinity of the origin. The other knots are evenly distributed in $x \in [-1, 1]$. The knot spacing at the center is $1/100000$ of the total length. Further decrease in this separation resulted in ill-conditioned matrices, and has no improvement on the results. .	45
4.4	The five lowest eigenenergies (E_1 - E_5) of the 1-D quantum box with $L_x = \pi$. The uniform grid cubic B -splines are used, and results are given for various number of basis functions N	46
4.5	The five lowest eigenenergies (E_1 - E_5) of the 1-D quantum box with $L_x = \pi$. The splines are expanded between $x = 0$ and $x = L_x$, and the first and the last splines are modified by Eq.4.2 to satisfy proper boundary conditions supplied by ordinary B -splines at $x = 0$ and $x = L_x$. The uniform grid cubic B -splines are used, and results are given for various number of basis functions N	48
4.6	The five lowest eigenenergies (E_1 - E_5) of the 1-D triangular quantum well for $k_x = 1$. The uniform grid cubic B -splines are expanded in the region $x \in [0, 10]$, and the results are given for various number of basis functions N	48

4.7	The five lowest eigenenergies (E_1 - E_5) of the 1-D triangular quantum well ($k_x = 1$) for various number of basis functions N . The uniform grid cubic B -splines are expanded in the region $x \in [0, 10]$, and the first basis in the expansion is modified to match the proper boundary conditions.	49
4.8	The multiscale expansion details of Eq. (3.9)	51
4.9	The results of multiscale expansion compared to the ordinary SFM	51
4.10	The knot spacing for non-uniform cubic B -Splines	53
4.11	The results of non-uniform grid cubic B -splines for $N = 159$ compared to multiresolution calculations for $N = 139$	53
4.12	The knot spacing for non-uniform cubic B -splines satisfying imposed boundary conditions. This non-uniform mesh together with extra $\tilde{B}(x)$ spline defines $N = 85$ basis functions.	56
4.13	The results of non-uniform grid cubic B -splines satisfying imposed boundary conditions at $x = 0$ for $N = 85$ compared to non-uniform grid cubic B -splines calculations for $N = 159$. Note that error percentage is less than second decimal place.	56
4.14	Three points and five points FDM results are compared with the SFM calculations for various N . Here N is the number of grid points in FDM and the number of basis functions in the SFM. The exact energies are $E_0 = -62.3953$, and $E_1 = -62.3928$	57
4.15	The six bound eigenenergies (E_1 - E_6) of the 1-D asymmetric double rectangular well potential with $V_{b,1} = 10$, $V_{b,2} = 15$, $b_1 = b_2 = 1$, $a_1 = 1$ and $a_2 = 2$. The uniform grid cubic B -splines are expanded in the region $x \in [-7, 7]$, and the results are given for various number of basis functions N	58
4.16	The six lowest eigenenergies (E_1 - E_6) of the 1-D double well potential with softened Coulomb attraction. The uniform grid cubic B -splines are expanded in the region $x \in [-25, 25]$, and the results are given for various number of basis functions N	59
4.17	Non-uniform grid mesh description of the double well potential with softened Coulomb attraction. Splines are expanded in the region $x \in [-25, 25]$, and total number of basis functions $N = 121$.	60
4.18	The six lowest eigenenergies (E_1 - E_6) of the 1-D double well potential with softened Coulomb attraction. The non-uniform grid mesh given in Table 4.17 is used.	60
4.19	Chemical potential and energy levels (meV) of [40].	61
4.20	Chemical potential and energy levels (meV) for Example 1, our calculations.	62

4.21	First bound energy level with various n_e	62
4.22	Some expectation values for the second example, $n_e = 6000/\mu\text{m}^2$.	62
4.23	The results of the self-consistent calculation for the third example; $V_b = 300\text{meV}$, and $\kappa = 13$	63
4.24	The results of the self-consistent calculation for the fourth example; $V_b = 300\text{meV}$, $\kappa = 13$, $N_{dep} = 800/\mu\text{m}^2$, and $N_A = 300/\mu\text{m}^2$	63
4.25	The SFM results for 2-D harmonic oscillator with $k_x = 1$, and $k_y = 1.21$ compared with the exact values.	64
4.26	The SFM results of 2-D quantum box of dimensions $L_x = \pi$ and $L_y = \pi/\sqrt{2}$ compared with the exact values. The proper B -splines are used at the box surface to satisfy the imposed boundary con- ditions.	65
4.27	The SFM results for 3-D harmonic oscillator for $k_x = k_y = k_z = 1$ compared with the exact values.	67
4.28	The SFM results of 3-D quantum box of dimensions $L_x = \pi$, $L_y = \pi/\sqrt{2}$ and $L_z = \pi/\sqrt{3}$ compared with the exact values. The proper B -splines are used at the box surface to satisfy the imposed boundary conditions.	69
4.29	The SFM results of finite quantum wire of dimensions $L_x = \pi$, $L_y = \pi/\sqrt{2}$ and $L_z = \pi/\sqrt{3}$. The proper B -splines are used at the box surface to satisfy the imposed boundary conditions. The impu- rity is taken at $(L_x/2, L_y/2, L_z/2)$ and $(L_x/2 + 2L_x/30, L_y/2, L_z/2)$ for the first and second examples, respectively. In both cases $l_x = 2L_x/15$, $l_y = 2L_y/15$, $l_z = 2L_z/15$, $N_x = N_y = N_z = 12$, and $N = 1728$	70

LIST OF FIGURES

2.1	A typical GaAs/Al _x Ga _{1-x} As single quantum well.	7
2.2	The SDRQW potential.	13
2.3	The ADRQW potential.	14
2.4	The double well potential with softened Coulomb attraction with $a = 0.1$	15
2.5	Charge transfer results in band bending at thermal equilibrium.	16
2.6	Conduction band edge profile (Top), ionized acceptor profile (Middle), and donor profile (Bottom)	19
2.7	Detailed conduction and valance band edge for heterojunction with p-type residual doping.	20
3.1	The cubic B -spline $B_0(x)$ centered at the origin.	26
3.2	Overlapping of cubic B -splines in Eq. (3.2) each one is centered at x_i . Why matrix elements $H_{i,j}$ and $S_{i,j}$ in Eq. (3.3) vanish for $ i - j > 3$ is clearly seen.	28
3.3	The cubic B -spline wavelet $W(x)$ defined in Eq. (3.10).	30
3.4	The non-uniform cubic B -spline $B(x)$ defined in Eq. (3.11) for $h_1 = x_2 - x_1 = 1/4$, $h_2 = x_3 - x_2 = 1/2$, $h_3 = x_4 - x_3 = 1$, and $h_4 = x_5 - x_4 = 2$	32
3.5	The H or S matrix elements of 8x8 mesh ($N = 64$). Non-zero matrix elements are shown by shaded boxes. In each row, the 2-D grid points are ordered from left to right.	39
3.6	The H or S matrix elements of 8x8 mesh ($N = 64$). Non-zero matrix elements are shown by shaded boxes. In each row, the 2-D grid points are ordered from left to right and right to left in subsequent rows alternatively.	40
4.1	The bound state wavefunction of the singular potential $V(x) = -10\delta(x)$	45
4.2	The wavefunction $\varphi(x)$ given in Eq. (3.9) is expanded up to various scales; (a) it is in the coarsest scale ($n = 0$), (b) it is expanded up to first detail scale ($n = 1$), and (c) it is expanded up to seventh detail scale ($n = 7$).	52

4.3	The wavefunction for the 2-D harmonic oscillator potential; $k_x = 1$, $k_y = 1.21$, $n_x = 0$, $n_y = 0$, $N_x = 10$, and $N_y = 10$	65
4.4	The wavefunction for the 2-D harmonic oscillator potential; $k_x = 1$, $k_y = 1.21$, $n_x = 1$, $n_y = 0$, $N_x = 10$, and $N_y = 10$	66
4.5	The wavefunction for the 2-D harmonic oscillator potential; $k_x = 1$, $k_y = 1.21$, $n_x = 0$, $n_y = 1$, $N_x = 10$, and $N_y = 10$	67
4.6	The wavefunction for the 2-D harmonic oscillator potential; $k_x = 1$, $k_y = 1.21$, $n_x = 2$, $n_y = 0$, $N_x = 10$, and $N_y = 10$	68
4.7	The ground state probability amplitude of the particle in the finite quantum wires (see Table 4.29). There is no impurity potential in the left-hand side plot, the right-hand side plot on the other hand is for Example 2.	71
4.8	The first excited state probability amplitude of the particle in the finite quantum wires (see Table 4.29). There is no impurity potential in the left-hand side plot, the right-hand side plot on the other hand is for Example 2.	72
4.9	The second excited state probability amplitude of the particle in the finite quantum wires (see Table 4.29). There is no impurity potential in the left-hand side plot, the right-hand side plot on the other hand is for Example 2.	72

CHAPTER 1

INTRODUCTION

The pioneering work of L. Esaki and R. Tsu [1] in 1969 and the development of revolutionary crystal growth techniques such as the molecular beam epitaxy have opened up a whole new world of low-dimensional physics and technology [2, 3, 4, 5, 6, 7, 8, 9, 10, 11, 12, 13, 14]. The motion of charge carriers in the resulting high quality low-dimensional structures such as quantum wells, wires and dots is restricted in one-, two- and three-dimensions (1-, 2-, and 3-D), respectively.

There is an ever increasing level of interest in these structures because of their importance for new device applications. For example, the technology of modulation doping made it possible to create very high mobility devices such as high-electron-mobility transistor (HEMT), two-dimensional electron-gas field effect transistor (TEGFET), quantum dot lasers, quantum well and dot infrared photodetectors are exciting new device applications [15, 16, 17, 18, 19, 20, 21, 22, 23, 24, 25, 26, 27, 28].

The low-dimensional semiconductor structures are also interesting because they usually offer unusual new physics. Quantum Hall effect, fractional quantum Hall effect, and quantized conductance in point contacts are just a few examples that created considerable excitement [29, 30, 31, 32, 33, 34, 35, 36, 37, 38, 39].

Proper understanding and design of new devices require theoretical, experimental and computational work. Especially important is to develop fast and accurate algorithms to solve the related equations, namely the Schrödinger equation and Poisson's equations [40, 41, 42, 43] reduced in appropriate dimensions.

The most widely used numerical techniques to solve the semiconductor equations are the *finite difference* (FDM) and the *finite element methods* (FEM) [44, 45]. They lead to structured, very sparse matrix representations of the underlying equations on meshes in real space [46]. The wavefunction and the electronic structure calculations of arbitrarily shaped semiconductors with arbitrary confining potential profile can be obtained without any a priori-knowledge about the solution.

The pioneering works in numerical solution of Schrödinger equation using FDM appeared at the beginning of 1930s [47, 48]. In this method, Schrödinger equation is discretized using Taylor-series expansion of the unknown wavefunction usually on regular Cartesian grids. Schrödinger equation is then converted into a simple eigenvalue matrix equation.

The FEM on the other hand was first proposed in 1943 by Courant [49] in an engineering application. Its use in physics goes back to the early 1980's.

The finite difference methods may be characterized as “local” in the sense that the solution in nearby points only. Thus, an initial estimate is required to let the algorithm started. The normalization should be performed later.

The use of basis sets, on the other hand, is very common in physics. This

transforms the solution of a differential equation into an algebraic eigenvalue problem. This approach is particularly popular because of tremendous developments in the field of computer technology. Nowadays, large matrices can be readily diagonalized with high accuracy in reasonably short computation times. By using dedicated sparse matrix algorithms, we achieved to use $N = 1,000,000$ basis functions using an ordinary personal computer.

The basis set method may be characterized as “global” in the sense that the solution at one point is linked to the solutions at all other points. Initial estimate is thus unnecessary.

Many types of basis sets have been used in solving equations that one faces within condensed matter physics. In this work, we focus on the use of B -splines which is a relatively new development in physics. Although B -splines were introduced by Schoenberg [50] in 1946, their application to the solution of differential equations took place two-decades later [51, 52, 53] and their use in description of an atomic system is first realized by Shore [54, 55, 56, 57, 58] in the beginning of 1970s. These basis functions become very popular after 1990s because of their very accurate representation of both discrete and continuum atomic states compared to more conventional L^2 basis sets. B -splines have also proved advantageous in simplifying the computation of many-body wavefunctions where one requires solution to coupled sets of integrodifferential equations [54] and thus suitable for self-consistent calculations.

The method we describe here is closely related with the FEM and we describe

it as “*spline function method*” (SFM). The SFM is an exact diagonalization of the Hamiltonian matrix using B -splines as basis set. Because of its efficiency, the SFM has been widely used in quantum chemistry since then but it is relatively new in condensed matter physics. The SFM is used only in one study [59] in that area. The same basis set is used by many others [60, 61, 62, 63, 64] in a variational manner where the expansion coefficients are used as variational parameters. The usually used uniform grid approach is applied to standard homogeneous boundary conditions for periodic, non-periodic, 1-D, 2-D and 3-D semiconductor electron systems using cubic B -spline basis set.

Another contribution in this thesis is the application of *the multiresolution analysis* (MRA) to a condensed matter physics problem. The MRA is a relatively recent approach which is first introduced in the late 1980s by Meyer [65, 66] and Mallat [67]. In the MRA, we used B -spline wavelets which were introduced by Chui [68] in 1991. Wavelets are very useful in many engineering applications including signal processing, data compression, and computer graphics. The wavelet basis functions are first used in electronic structure calculations [69] in 1993. Their use in physics is not so widespread and almost all works are limited to applications in atomic and molecular physics (see Arias [70] for an extensive review).

The thesis is organized as follows: The formulation of the problem of low-dimensional semiconductor structures is given in Chapter 2. Here the aim is to give some minimal information on the physical problems that will be solved using

B-spline basis approach. The Chapter 3 is devoted to an extensive presentation of the problems. An attempt is made to compare various different methods. The results are presented in Chapter 4. The superiority of our new method is shown in that chapter by comparing its results with those that are obtained by using other methods. Finally, our conclusion is presented in Chapter 5 which includes an analysis of pros and cons of the new approach.

As we are interested in applying the spline function method to a set of different problems in low-dimensional quantum structures, we now turn to a discussion of possible examples.

CHAPTER 2

LOW-DIMENSIONAL SEMICONDUCTOR STRUCTURES

2.1 Introduction

Low-dimensional semiconductor structures are realized by quantum confinement of the carrier motion. Carrier confinement results in discrete energy levels associated with the motion along the directions where the carrier motion is restricted. The first demonstration of formation of discrete energy levels in artificial confinement is given in Si metal oxide semiconductor structure [71]. The carrier confinement is achieved basically in three ways; these are geometrical, electrostatic, and compositional confinement. In geometrical confinement, one or more dimensions of the structure are made considerably small by a suitable etching or growth technique. In this way, the carrier motion is restricted along these directions. In electrostatic confinement, electric field is used to confine the charge carriers. The carriers are attracted and confined by a suitable electric field in the vicinity of grating gates, narrow gates, split gates, or other variants. The strength of the confinement, on the other hand, can be adjusted by the applied voltage dynamically. Compositional confinement on the other hand is due to the resultant potential barriers caused by the band-gap offset at the interface of two

materials whose chemical composition is different. Two common examples are the Si/SiO₂ and GaAs/Al_xGa_{1-x}As interfaces. The barrier heights are 3eV and 0.3eV (for $x = 0.3$), respectively. Compositional confinement opens the way of manufacturing very interesting and unusual electronic devices that can be created by growing alternating layers of high and low band gap energy materials over an intrinsic substrate. The result is the generation of “quantum wells” where electrons can now reside. Since the carrier motion is restricted in only one dimension, these systems are regarded as two-dimensional. If we create only one GaAs layer between two GaAlAs layers (Fig. 2.1) there will be a single quantum well. If there is a large number of quantum wells grown on top of each other, one has a superlattice.

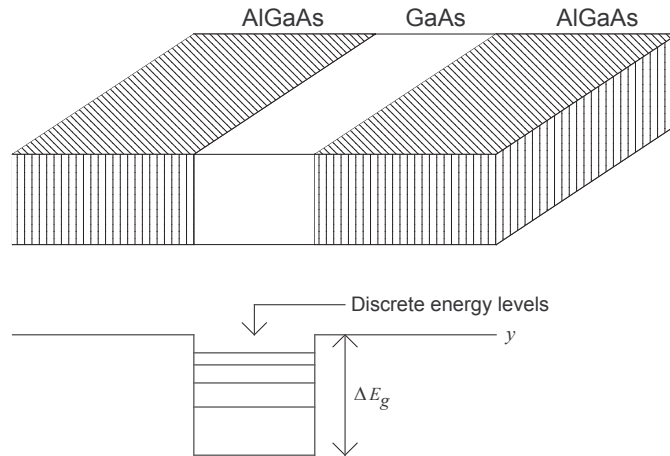


Figure 2.1: A typical GaAs/Al_xGa_{1-x}As single quantum well.

If the electron motion is restricted in two dimensions, resultant configuration is called as “quantum well wire (QWW)”. Such systems are usually generated from quantum wells. One of the degrees of freedom is restricted usually by wet

or dry etching techniques. Quantum wires are one-dimensional systems because charge carriers are free to move only in one-dimension. If movement is further restricted in all directions, the resultant configuration is known as “quantum dot” or “artificial atom”. Quantum dot structures are realized if one extends the lateral confinement of the wire structures to the remaining degree of freedom of the carriers [40].

2.2 Modulation Doping

High mobility is achieved by the spatial separation between the carriers and their parent donors or acceptors. This separation reduces Coulomb scattering and therefore increases mobility. Such a separation and resultant high mobility of carriers can be achieved by a process known as “modulation” or “selective” doping [72, 73, 74, 75, 76, 77, 78, 79, 80]. The transistors based on modulation doping are known as MODFETs or HEMTs. Basic compound semiconductor material is GaAs/ $\text{Al}_x\text{Ga}_{1-x}\text{As}$. If the high band gap material is doped with donor atoms, electrons diffuse over to the quantum wells of the low band gap GaAs layers. Since the GaAs is free of impurity atoms, the electrons do not encounter any impurity scatterers. This leads to a reduction in electron impurity scattering, thus to a substantial increase in electron mobility. Research in implementing MODFET type transistors is now being extended to other compound semiconductor materials. One such material is InP based alloys where peak electron velocity is higher than that in GaAs [81].

Another novel doping scheme is delta-doping which refers to the technique by which dopant atoms are confined to a single atomic plane within the semiconductor.

2.3 Wavefunction Engineering

Advanced crystal growth techniques and various doping schemes opened a new engineering area: “Wavefunction engineering” which refers to the ability of specifying the localization of carrier wavefunctions in heterostructures through control over the material composition, growth, and the geometry. Wavefunction engineering made it possible to create almost arbitrarily featured enhanced semiconductor devices. Their realization starts with the design of carrier wavefunctions and electronic structure. These involve designing of concentration of carriers such that the probability of being present in specific regions or layers results in an increase in mobility. This further involves shaping of overlap of carrier wavefunctions to enhance the transport properties, designing potential profiles to engineer optical spectra, and to determine electronic energy levels or any other related physical properties.

Shape of the potential profile also depends on the presence of free carriers. Location of these carriers modify the potential profile. There is always a feedback between carrier density and the confining potential. This feedback usually requires a self-consistent solution of Schrödinger’s and Poisson’s equations. However this requirement is not valid for single electron calculations, where the

confining potential is known and fixed.

After this general introduction, we now should turn to a discussion of the model systems that we investigate by using the SFM. The information given here will be the input to our calculations. We also provide the analytical solutions, wherever they are available for the purpose of comparison with our results.

2.4 Possible Potential Profiles: Model Problems

In the following, we give the minimal information on the 1-D, 2-D and 3-D problems on that order. Unless otherwise stated, all quantities are given in atomic units ($\hbar = 1$ and $m = 1$).

2.4.1 The 1-D Harmonic Oscillator

The 1-D harmonic oscillator confining potential is given by,

$$V(x) = \frac{1}{2}(k_x x^2), \quad (2.1)$$

where k_x maybe taken as an arbitrary real positive constant. The exact eigenvalues are,

$$E(n_x) = \sqrt{k_x}(n_x + \frac{1}{2}), \quad n_x = 0, 1, 2 \dots \quad (2.2)$$

2.4.2 The Attractive δ Potential

Delta-doping refers to the technique by which dopant atoms are confined to a single atomic plane within the semiconductor. The resultant potential profile at

the dopant plane ($x = x_0$) can simply be represented by a Dirac-delta function of the form,

$$V(x) = -V_0\delta(x - x_0), \quad (2.3)$$

where the magnitude V_0 depends on the dopant concentration. Such an 1-D attractive potential has only one bound state and its exact energy is given by [82, 83],

$$E_0 = -\frac{V_0^2}{2}. \quad (2.4)$$

The well-known other forms of δ potential are,

$$\delta(x) = \lim_{\epsilon \rightarrow 0} \frac{1}{\pi} \left(\frac{\epsilon}{x^2 + \epsilon^2} \right), \quad (2.5)$$

$$\delta(x) = \lim_{\epsilon \rightarrow 0} \frac{1}{\sqrt{\pi\epsilon}} e^{-\frac{x^2}{\epsilon}}, \quad (2.6)$$

and

$$\delta(x) = \lim_{\epsilon \rightarrow 0} \begin{cases} \frac{1}{\epsilon} & \text{for } |x| \leq \frac{\epsilon}{2} \\ 0 & \text{otherwise} \end{cases}. \quad (2.7)$$

“As a physical model, delta-function potential has been used to represent a localized potential whose energy scale is greater than any other and whose spatial extension is smaller than all other length scales [84].”

2.4.3 The 1-D Quantum Box

The 1-D quantum box confining potential is,

$$V(x) = \begin{cases} 0 & \text{for } 0 \leq x \leq L_x \\ \infty & \text{otherwise} \end{cases}, \quad (2.8)$$

and its eigenenergies are given by,

$$E(n_x) = \frac{\pi^2 n_x^2}{2 L_x^2}, \quad n_x = 1, 2, 3 \dots \quad (2.9)$$

where L_x is the box length.

2.4.4 The 1-D Triangular Quantum Well

The 1-D triangular quantum well confining potential is defined as,

$$V(x) = \begin{cases} k_x x & \text{for } x \geq 0 \\ \infty & \text{otherwise,} \end{cases} \quad (2.10)$$

where k_x is an arbitrary real positive constant. Its eigenfunctions are Airy functions and the exact eigenenergies are the roots of these Airy functions. The lowest five eigenenergies for $k_x = 1$ are given in Table 2.1.

Table 2.1: The lowest five eigenenergies of the 1-D triangular quantum well confining potential for $k_x = 1$ defined in Eq. (2.10).

E_1	E_2	E_3	E_4	E_5
1.8557571	3.2446076	4.3816712	6.3052630	5.3866138

2.4.5 The Symmetric Double Rectangular Quantum Well

The symmetric rectangular double quantum well (SDRQW) potential is given by,

$$V(x) = \begin{cases} V_b & \text{for } b \leq |x| \leq a + b \\ \infty & \text{for } |x| > A \\ 0 & \text{otherwise,} \end{cases} \quad (2.11)$$

and plotted in Fig. 2.2. Basis functions are expanded between $x = -A$ and $x = A$.

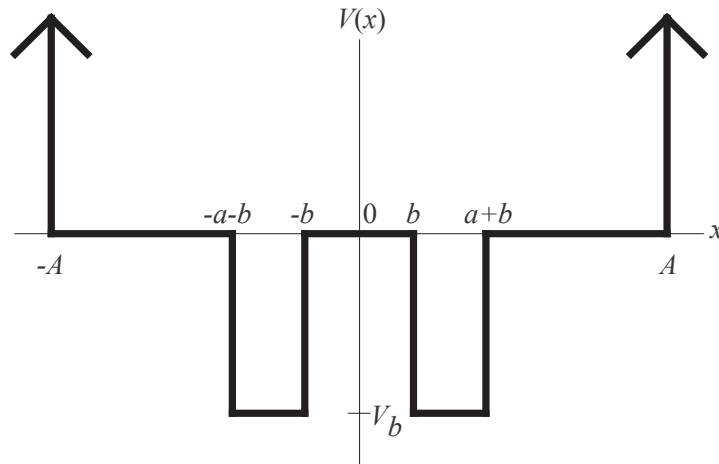


Figure 2.2: The SDRQW potential.

2.4.6 The Asymmetric Double Rectangular Quantum Well

The asymmetric double rectangular quantum well (ADRQW) potential is given by,

$$V(x) = \begin{cases} V_{b,1} & \text{for } -a_1 - b_1 \leq x \leq -b_1 \\ V_{b,2} & \text{for } b_2 \leq x \leq a_2 + b_2 \\ \infty & \text{for } x < -A_1 \text{ or } x > A_2 \\ 0 & \text{otherwise,} \end{cases} \quad (2.12)$$

and plotted in Fig. 2.3. Basis functions are expanded between $x = -A_1$ and $x = A_2$.

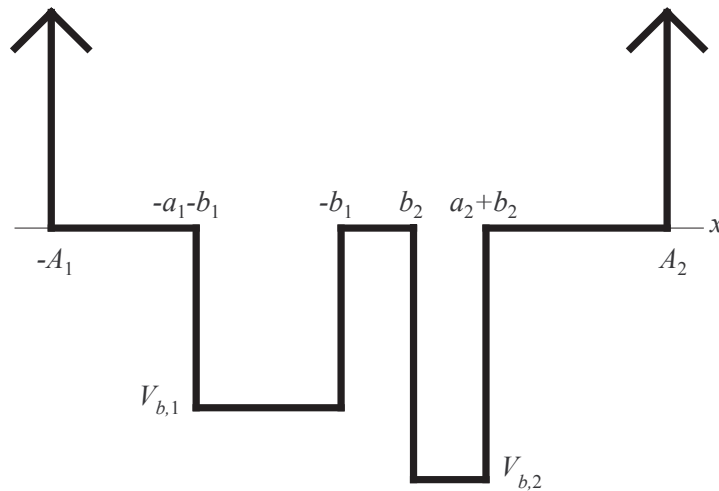


Figure 2.3: The ADRQW potential.

2.4.7 The Double Quantum Well with Softened Coulomb Attraction

A double well potential with softened Coulomb attraction [85] at $x = \pm 1/2$ is plotted in Fig. 2.4 and is given by,

$$V(x) = -\frac{1}{\sqrt{(x - 1/2)^2 + a^2}} - \frac{1}{\sqrt{(x + 1/2)^2 + a^2}}. \quad (2.13)$$

The lowest six exact eigenenergies for $a = 0.1$ are tabulated in Table 2.2.

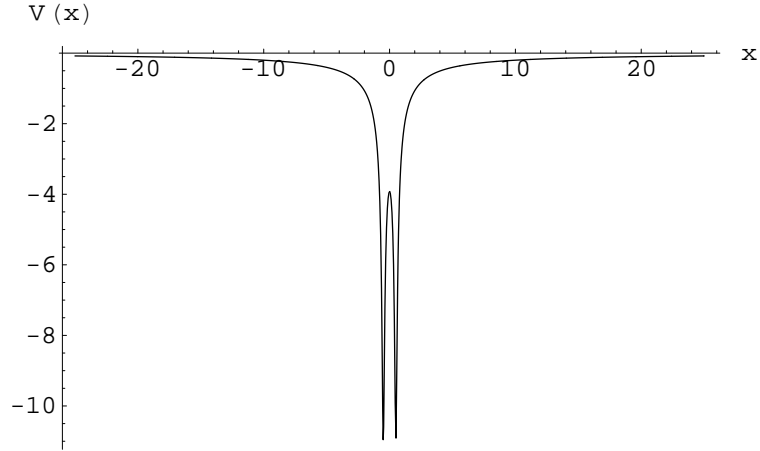


Figure 2.4: The double well potential with softened Coulomb attraction with $a = 0.1$.

Table 2.2: The lowest six exact eigenenergies of the double well potential with softened Coulomb attraction given in Eq. (2.13) for $a = 0.1$.

E_1	E_2	E_3	E_4	E_5	E_6
-5.53663095	-3.90370790	-0.83649017	-0.60657639	-0.30697893	-0.24825966

Up to now, we have presented the model systems. We now turn to a discussion of a more realistic system. In modulation doped heterojunctions the calculation should be done self-consistently.

2.4.8 The Modulation Doped Heterojunction

In the following, computational details and relying assumptions about the electronic structure calculations of the modulation doped heterojunction are based on Bastard's work [41].

Confining potential causes size quantization of carrier motion in x direction. This quantization restricts the motion along x . But motion in y and z directions are free and we can consider such a structure as a two-dimensional electron gas (2-DEG).

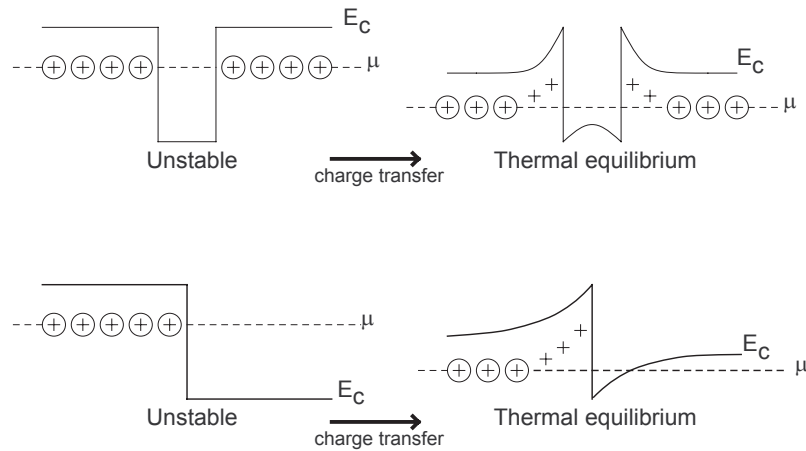


Figure 2.5: Charge transfer results in band bending at thermal equilibrium.

A very important advantage of modulation doping is the tremendous improvement in the mobility. It is achieved by the spatial separation between the carriers and their parent donors. Further separation can take place by inserting a spacer layer between the donors and the quasi bi-dimensional electron gas. Spacer part is the undoped part in the barrier.

Actual heterojunctions contain residual impurities. N_d donors per unit volume

are created in the barrier. Assuming that p type residual doping exists, then N_A acceptors per unit volume remains in the channel, and $N_{b,A}$ acceptors per unit volume remains in the barrier. These are unwanted residuals and they not only degrade the mobility but also change the energy levels, and thus the amount of charge transferred.

In the following, the steps of the self-consistent calculations are explained in detail.

2.4.8.1 Self Consistent Calculations

We have a many body problem which involves electron-electron interaction. The simplest approximation to this problem is that of Hartree's. In this approximation the exact many body interaction is replaced by an average one. Each electron is assumed to move in a self-consistent potential $\phi_{sc}(\vec{r})$ which is created by all other particles, and we have to solve the coupled Poisson's and Schrödinger's equations,

$$\nabla^2 \phi_{sc}(\vec{r}) = \frac{e}{\kappa} \left[\sum_{\alpha, \text{occupied}} |\varphi_{\alpha}(\vec{r})|^2 - \sum_{\vec{R}_{don}} \delta(\vec{r} - \vec{R}_{don}) + \sum_{\vec{R}_{acc}} \delta(\vec{r} - \vec{R}_{acc}) \right], \quad (2.14)$$

and

$$\left[-\frac{\hbar^2}{2m(x)} \left(\frac{\partial^2}{\partial y^2} + \frac{\partial^2}{\partial z^2} \right) - \frac{\hbar^2}{2} \frac{\partial}{\partial x} \frac{1}{m(x)} \frac{\partial}{\partial x} + V_b(x) - e\phi_{sc}(\vec{r}) \right] \varphi_{\alpha}(\vec{r}) = E_{\alpha} \varphi_{\alpha}(\vec{r}), \quad (2.15)$$

where κ is the relative dielectric constant of the channel, and assumed as the same in the barrier since penetration depth of the wavefunction is quite small.

\vec{R}_{acc} and \vec{R}_{don} are the position vectors of the ionized acceptors and donors. The average number of ionized donors and acceptors per unit volume are given by,

$$N_d^+(x) = \frac{1}{\mathcal{V}} \int \delta(\vec{r} - \vec{R}_{don}) d^3 R_{don}, N_a^-(x) = \frac{1}{\mathcal{V}} \int \delta(\vec{r} - \vec{R}_{acc}) d^3 R_{acc}, \quad (2.16)$$

where \mathcal{V} is the macroscopic volume. Using these average values and reducing the equations for one-dimensional case within the Hartree approximation one obtains,

$$\left[-\frac{\hbar^2}{2} \frac{\partial}{\partial x} \frac{1}{m(x)} \frac{\partial}{\partial x} + V_b(x) - e\phi_{sc}(x) \right] \varphi_i(x) = E_i \varphi_i(x), \quad (2.17)$$

and

$$\frac{d^2 \phi_{sc}(x)}{dx^2} = \frac{e}{\kappa} \left[\sum_{i, occupied} n_i \varphi_i^2(x) - N_d^+(x) + N_a^-(x) \right]. \quad (2.18)$$

Here, n_i labels the areal concentration of electrons in the i 'th subband, which is related to temperature T , and the chemical potential μ by,

$$n_i = \frac{m_i k_B T}{\pi \hbar^2} \ln(1 + e^{\frac{\mu - E_i}{k_B T}}). \quad (2.19)$$

Here, k_B is the Boltzmann constant. For $T = 0$, Eq. (2.19) reduces to,

$$n_i = \frac{m_i}{\pi \hbar^2} (\mu - E_i) U(\mu - E_i), \quad (2.20)$$

where $U(x)$ is the unit step function. $U(x) = 0$ for $x < 0$ and 1 otherwise. Charge neutrality of the heterojunction requires,

$$\frac{\kappa}{e} \frac{d\phi_{sc}(x)}{dx} \Big|_{-\infty}^{\infty} = \sum_{i, occupied} n_i + \int_{-\infty}^{+\infty} dx [N_a^-(x) - N_d^+(x)] = 0. \quad (2.21)$$

This equation is obtained by integrating Eq. (2.18). Eq. (2.21) also requires $-\phi'_{sc}(x = \infty) = -\phi'_{sc}(x = -\infty) = 0$, since no electric field exists far away from the interface. It should be noted that primes indicate derivatives with respect to its argument x , and this corresponds to the electric field.

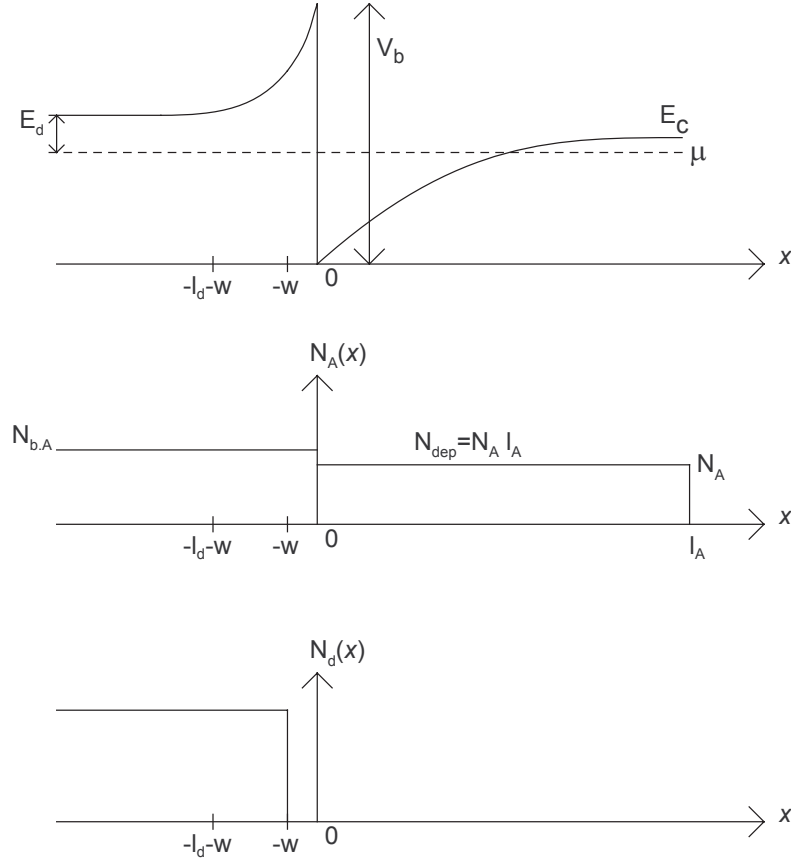


Figure 2.6: Conduction band edge profile (Top), ionized acceptor profile (Middle), and donor profile (Bottom)

Heterojunction is also in thermodynamical equilibrium. Chemical potential μ should be the same everywhere. For a residual p-type doping of the channel, μ coincides with the acceptor level in the channel and donor level in the barrier far away from the junction,

$$\mu = E_v(x = +\infty) + E_A = E_c(x = -\infty) + E_d, \quad (2.22)$$

where E_A is the binding energy of acceptors in the channel and E_d is the binding energy of donors in the barrier.

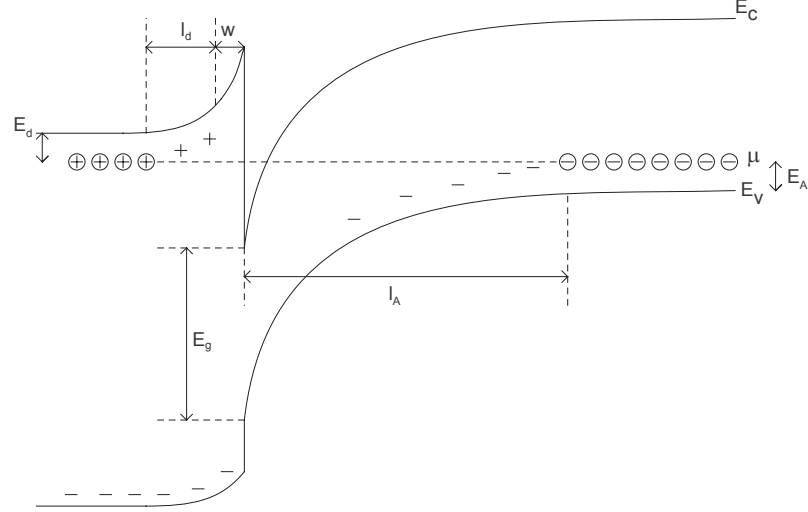


Figure 2.7: Detailed conduction and valance band edge for heterojunction with p-type residual doping.

The $\phi_{sc}(x)$ in Eq. (2.18) may be written as,

$$\phi_{sc}(x) = \phi_{e-e}(x) + \phi_A(x) + \phi_d(x) + \phi_w(x), \quad (2.23)$$

where $\phi_{e-e}(x)$ is the electron-electron interaction term, $\phi_A(x)$ is caused by ionized acceptors N_A^- , $\phi_d(x)$ is due to the ionized donors N_d^+ and residual ionized acceptors $N_{b,A}^+$ in the barrier, and $\phi_w(x)$ is the potential in the undoped spacer region. Eq. (2.18) must be integrated twice with suitable boundary conditions in order to obtain $\phi_{sc}(x)$.

The depletion length assumption may simplify the calculations. As a first approximation, all channel acceptors may be taken as ionized between $x = 0$ and $x = l_A$. For $x > l_A$ they may be taken as neutral. If we assume that band is flat for $x > l_A$ then we have for the potential due to channel acceptors,

$$\phi'_A(x = l_A) = 0, \quad (2.24)$$

and by taking zero potential at $x = 0$,

$$\phi_A(x = 0) = 0. \quad (2.25)$$

Using these boundary conditions and integrating Eq. (2.18) twice, one obtains,

$$\phi_A(x) = \frac{e}{2\kappa} N_A^- x(x - 2l_A). \quad (2.26)$$

The doped part of the barrier is the region between $x = -\infty$ and $x = -w$. Here w is the spacer layer thickness. Similar assumptions can be made for doped part of the barrier. $\phi_d(x)$ is the potential due to donors (N_d) and residual acceptors ($N_{b,A}$) in the barrier. Between $x = -l_d - w$ and $x = -l_d$ all donors are ionized. Electric field at $x = -\infty$ is zero, and beyond $x = -l_d - w$ the potential profile is flat, thus the electric field is also zero at $x = -l_d - w$. These yield,

$$\phi_d(x) = -\frac{e}{2\kappa} (N_d^+ - N_{b,A}^+) (x + l_d + w)^2 + \phi_0, \quad (2.27)$$

where ϕ_0 ensures the continuity of the potential at $x = -w$. Within the depletion length assumption, the charge neutrality Eq. (2.21) now reads,

$$N_d l_d = \sum_{i, \text{occupied}} n_i + N_{dep} + N_{b,A}(w + l_d), \quad (2.28)$$

where $N_{dep} = N_A^- l_A$. Here, l_d is still unknown and must be determined self-consistently.

The potential in the spacer part $\phi_w(x)$ is also determined by the equation,

$$\phi_w(x) = -|\vec{E}_0| x + \phi_1, \quad (2.29)$$

where $|\vec{E}_0|$ is constant and equal to the value of electric field along x at $x = 0$, and ϕ_1 is a constant to ensure continuity of the electrostatic potential.

In Eq. (2.29), no net charge in the interval of w is assumed. Furthermore, since w is small, electric field is assumed to be constant in the interval w . With these assumptions, $|\vec{E}_0| = \frac{\epsilon}{\kappa} N_{dep}$ and it is solely due to N_{dep} .

2.4.9 Two-Dimensional Single Electron Potentials

Here, we consider only the two simplest cases of 2-D confining potentials; the 2-D-harmonic oscillator and the 2-D quantum box.

2.4.9.1 The 2-D Harmonic Oscillator

The general 2-D harmonic oscillator potential is given by,

$$V(x, y) = \frac{1}{2}(\sqrt{k_x}x^2 + \sqrt{k_y}y^2), \quad (2.30)$$

where k_x and k_y may be taken as arbitrary real positive constants. The exact eigenvalues are,

$$E(n_x, n_y) = k_x\left(n_x + \frac{1}{2}\right) + k_y\left(n_y + \frac{1}{2}\right), \quad n_x, n_y = 0, 1, 2 \dots \quad (2.31)$$

2.4.9.2 The 2-D Quantum Box

The 2-D quantum box confining potential is,

$$V(x, y) = \begin{cases} 0 & \text{if } 0 \leq x \leq L_x \text{ and } 0 \leq y \leq L_y \\ \infty & \text{otherwise} \end{cases}, \quad (2.32)$$

and its eigenenergies are given by,

$$E(n_x, n_y) = \frac{\pi^2}{2} \left(\frac{n_x^2}{L_x^2} + \frac{n_y^2}{L_y^2} \right), \quad n_x, n_y = 1, 2, 3 \dots \quad (2.33)$$

where L_x and L_y are the box lengths.

We now turn to a discussion of three-dimensional cases.

2.4.10 Three-Dimensional Single Electron Potentials

In this section, only the two simplest cases; 3-D-harmonic oscillator and the 3-D quantum box are considered.

2.4.10.1 The 3-D Harmonic Oscillator

The general 3-D harmonic oscillator is given by,

$$V(x, y, z) = \frac{1}{2}(\sqrt{k_x}x^2 + \sqrt{k_y}y^2 + \sqrt{k_z}z^2), \quad (2.34)$$

where k_x , k_y and k_z maybe taken as arbitrary real positive constants. The exact eigenvalues are,

$$E(n_x, n_y, n_z) = k_x(n_x + \frac{1}{2}) + k_y(n_y + \frac{1}{2}) + k_z(n_z + \frac{1}{2}), \quad n_x, n_y, n_z = 0, 1, 2 \dots \quad (2.35)$$

2.4.10.2 The 3-D Quantum Box

The 3-D quantum box confining potential,

$$V(x, y, z) = \begin{cases} 0 & \text{if } 0 \leq x \leq L_x, \quad 0 \leq y \leq L_y \text{ and } 0 \leq z \leq L_z \\ \infty & \text{otherwise} \end{cases}, \quad (2.36)$$

and its eigenenergies are given by,

$$E(n_x, n_y, n_z) = \frac{\pi^2}{2} \left(\frac{n_x^2}{L_x^2} + \frac{n_y^2}{L_y^2} + \frac{n_z^2}{L_z^2} \right), \quad n_x, n_y, n_z = 1, 2, 3 \dots \quad (2.37)$$

where L_x , L_y and L_z are the box lengths.

As we now have completed the introduction of some problems that are solvable by SFM, we turn to a discussion of our method of solution.

CHAPTER 3

THE METHOD

3.1 Solution of One-Dimensional Schrödinger Equation

The one electron, one-dimensional (1-D) Schrödinger equation is given by,

$$-\frac{1}{2m^*} \frac{\partial^2}{\partial x^2} \varphi(x) + V(x) \varphi(x) = E \varphi(x), \quad (3.1)$$

where m^* is the isotropic effective mass, and $V(x)$ is the general one electron confining potential.

The unknown wavefunction $\varphi(x)$ in Eq. (3.1) is expanded in terms of a finite number N of basis functions $\beta_i(x)$ as,

$$\varphi(x) = \sum_{i=1}^N \alpha_i \beta_i(x). \quad (3.2)$$

The Schrödinger equation can be converted into a matrix equation most efficiently by using the Galerkin's treatment (basis and testing functions are the same). The wavefunction expansion Eq. (3.2) is substituted into the Schrödinger equation, and after taking inner products with testing functions, the matrix equation of the following form is obtained,

$$\mathbf{H}\alpha = E\mathbf{S}\alpha. \quad (3.3)$$

Here \mathbf{H} is the Hamiltonian matrix, \mathbf{S} is the overlap matrix, E is the eigenenergy and α is the eigenvector whose components are the expansion coefficients. The matrix elements of Eq. (3.3) are,

$$\begin{aligned} H_{i,j} &= -\frac{1}{2m^*} \int \mathfrak{B}_i(x)\mathfrak{B}_j''(x)dx + \int \mathfrak{B}_i(x)V(x)\mathfrak{B}_j(x)dx \\ S_{i,j} &= \int \mathfrak{B}_i(x)\mathfrak{B}_j(x)dx \end{aligned} \quad (3.4)$$

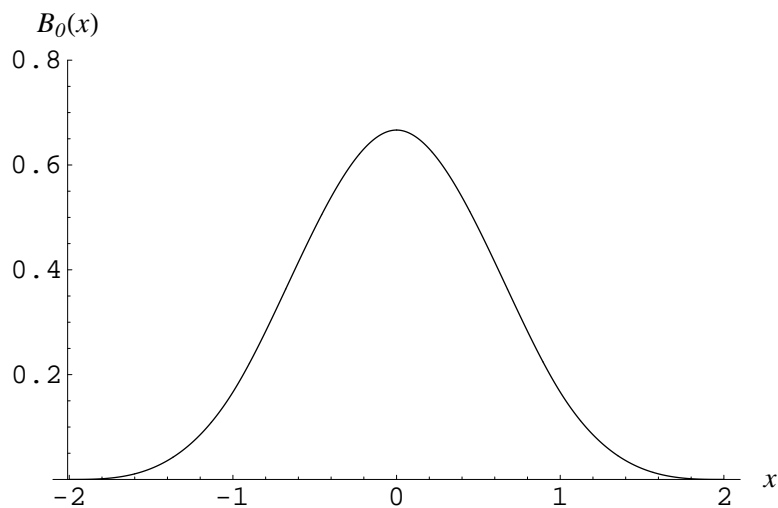


Figure 3.1: The cubic B -spline $B_0(x)$ centered at the origin.

The B -spline functions are used as the basis set. These splines are designed to have minimal support, provide bases for certain spline spaces, and are therefore called B -splines (*Basis*-splines). Splines are piecewise polynomial curves that are differentiable up to a prescribed order. Therefore all the integrals in the matrix elements can be evaluated exactly if $V(x)$ is analytically integrable. In this case,

an exact integration table is formed only once before the matrix filling procedure. This significantly improves the run-time because no integration process takes place during the execution. But, if $V(x)$ is not analytically integrable, a numerical integration process should take place during the run-time just for the $\int \beta_i(x)V(x)\beta_j(x)dx$ term.

B -splines are non-negative functions and therefore the expansion coefficients of an arbitrary function are close to the function values at the knots. This means that wild oscillations in the coefficients are avoided, cancellation errors are minimal and numerical stability is maximal [86].

The splines can be generated by the following general recursive relation,

$$B_i^k(x) = \left(\frac{x - x_i}{x_{i+k} - x_i}\right)B_i^{k-1}(x) + \left(\frac{x_{i+k+1} - x}{x_{i+k+1} - x_{i+1}}\right)B_{i+1}^{k-1}(x) \quad (k \geq 1), \quad (3.5)$$

with,

$$B_i^0(x) = \begin{cases} 1 & \text{if } x_i \leq x < x_{i+1} \\ 0 & \text{otherwise} \end{cases}, \quad (3.6)$$

where x_i 's are the knot points, and k is the spline order. It should be noted that the superscript k which stands for the spline order is dropped during the remaining of the text for the sake of simplicity. As an example for B -splines, a cubic B -spline $B_0(x)$ with uniform knot spacing, centered at origin is given by,

$$B_0(x) = \frac{1}{6} \begin{cases} (2 - |x|)^3 & \text{if } 1 \leq |x| < 2 \\ (2 - |x|)^3 - 4(1 - |x|)^3 & \text{if } 0 \leq |x| < 1 \\ 0 & \text{otherwise} \end{cases} , \quad (3.7)$$

and is plotted in Fig. 3.1.

The overlap of cubic B -splines are shown in Fig. 3.2. Since B -splines are symmetric and compactly supported, \mathbf{H} and \mathbf{S} matrices are real symmetric and highly sparse in nature. For a non-periodic confining potential $V(x)$, these matrices reduce to banded form with a bandwidth of $2k + 1$. But unfortunately this simple banded form is not the general case for the solution of two- or three-dimensional Schrödinger equations.

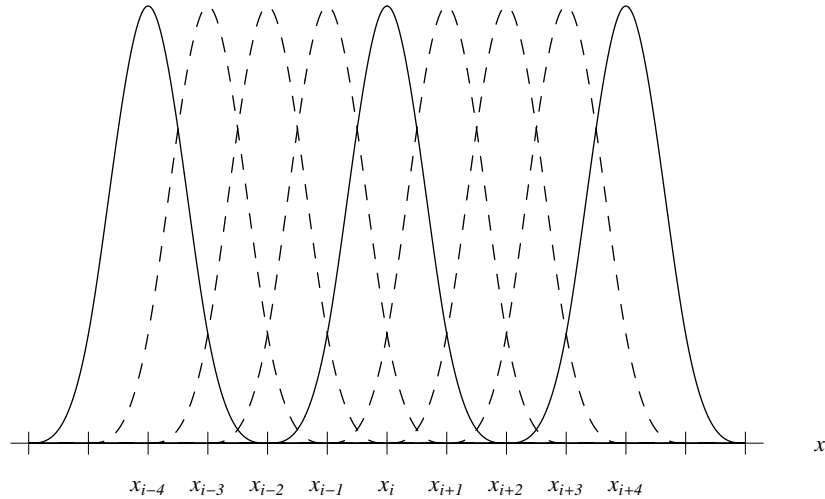


Figure 3.2: Overlapping of cubic B -splines in Eq. (3.2) each one is centered at x_i . Why matrix elements $H_{i,j}$ and $S_{i,j}$ in Eq. (3.3) vanish for $|i - j| > 3$ is clearly seen.

3.2 The Multiresolution Analysis Using Cubic B -Spline Wavelets

The mathematical theory underlying wavelet analysis is beyond the scope of this study. For interested readers, two excellent introductory books [87, 88] on wavelets are given in the references.

In multiresolution analysis, wavelet bases can efficiently represent functions on different scales. The represented function is expanded in terms of coarse-scale (scaling functions) and fine-scale basis (wavelet functions). The scaling functions represents the smooth variations whereas rapid variations or details are described by the wavelets. A smooth variation results in quite small wavelet coefficients, and can be ignored for most of the practical applications. This property is called as “*compression*” and enables a compact representation. The scaling functions $B(x)$ and their wavelets $W(x)$ are perpendicular to each other in all scales;

$$\int B(x)W(2^n x)dx = 0, \quad n = 0, 1, 2\dots \quad (3.8)$$

This property and compression allows an effective sparse matrix representation of the problem. The unknown wavefunction’s multiscale expansion in terms of cubic B -splines is given as,

$$\varphi(x) = \underbrace{\sum_{i=1}^{N^{(0)}} \alpha_i^{(0)} B_i(x)}_{\text{coarsest scale 0}} + \underbrace{\sum_{i=1}^{N^{(1)}} \alpha_i^{(1)} W_i(x)}_{\text{detail scale 1}} + \underbrace{\sum_{i=1}^{N^{(2)}} \alpha_i^{(2)} W_i(2x)}_{\text{detail scale 2}} + \underbrace{\sum_{i=1}^{N^{(3)}} \alpha_i^{(3)} W_i(4x)}_{\text{detail scale 3}} + \dots \quad (3.9)$$

Here, $B(x)$ ’s are the cubic B -splines, α ’s are the expansion coefficients, $N^{(0)}$,

$N^{(1)}, N^{(2)}, \dots$ are the number of basis functions used in the corresponding scale ($N = N^{(0)} + N^{(1)} + N^{(2)} + \dots$), and the cubic B -spline wavelet $W(x)$ is plotted in Fig. 3.3 and given by,

$$\begin{aligned}
W(x) = & -\frac{1}{40320}B(2x) + \frac{31}{10080}B(2x - 1) - \frac{559}{13440}B(2x - 2) + \frac{247}{1260}B(2x - 3) \\
& -\frac{9241}{20160}B(2x - 4) + \frac{337}{560}B(2x - 5) - \frac{9241}{20160}B(2x - 6) + \frac{247}{1260}B(2x - 7) \\
& -\frac{559}{13440}B(2x - 8) + \frac{31}{10080}B(2x - 9) - \frac{1}{40320}B(2x - 10)
\end{aligned} \tag{3.10}$$

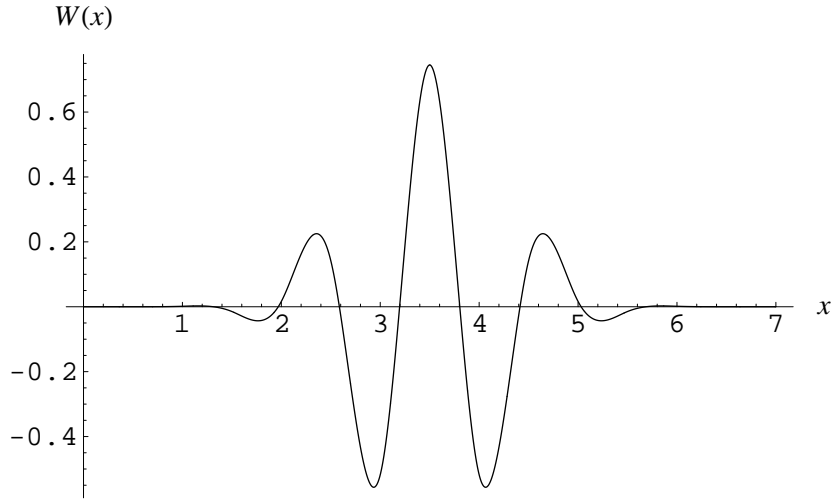


Figure 3.3: The cubic B -spline wavelet $W(x)$ defined in Eq. (3.10).

A similar procedure is applied to obtain the matrix equation in the form of Eq. (3.3). The unknown wavefunction is expanded as given in Eq. (3.9), and the testing functions include both B -splines and their wavelets. The resultant \mathbf{H} and \mathbf{S} matrices are sparse, but they are differently structured than the previous single scale expansion case. For a non-periodic confining potential $V(x)$, these matrices now consist of not a single, but many real symmetric banded sub-matrices.

3.3 Construction of Non-Uniform Grid B -Splines

Splines are flexible curves and may easily be modified to arbitrary knot spacing. A B -spline of order k is constructed of piecewise polynomials of order k on $k + 1$ consecutive regions which are a member of continuity class C^k with minimum support. It is always positive in these regions and identically zero elsewhere. As an illustrative example, consider a cubic B -spline (see Fig. 3.4) defined on four different knot spacing segments ($h_1, h_2, h_3,$ and h_4) as,

$$B(x) = \begin{cases} c_1 + c_2 \frac{x}{h_1} + c_3 \left(\frac{x}{h_1}\right)^2 + c_4 \left(\frac{x}{h_1}\right)^3 & \text{for } 0 \leq |x| < h_1 \\ c_5 + c_6 \frac{x}{h_2} + c_7 \left(\frac{x}{h_2}\right)^2 + c_8 \left(\frac{x}{h_2}\right)^3 & \text{for } h_1 \leq |x| < h_2 \\ c_9 + c_{10} \frac{x}{h_3} + c_{11} \left(\frac{x}{h_3}\right)^2 + c_{12} \left(\frac{x}{h_3}\right)^3 & \text{for } h_2 \leq |x| < h_3 \\ c_{13} + c_{14} \frac{x}{h_4} + c_{15} \left(\frac{x}{h_4}\right)^2 + c_{16} \left(\frac{x}{h_4}\right)^3 & \text{for } h_3 \leq |x| < h_4 \\ 0 & \text{elsewhere} \end{cases} \quad (3.11)$$

There are a total of sixteen equations for the sixteen unknowns c_{1-16} . Nine equations for the C^2 continuity of the spline across the consecutive segments, plus six homogeneous boundary conditions for $B(x) = B'(x) = B''(x) = 0$ at the two end points, and one additional normalization equation for the B -spline.

3.4 Construction of B -Splines Satisfying Arbitrary Boundary Conditions

Splines can be constructed by imposing arbitrary boundary conditions at the boundaries by using the method mentioned in the previous section. But these

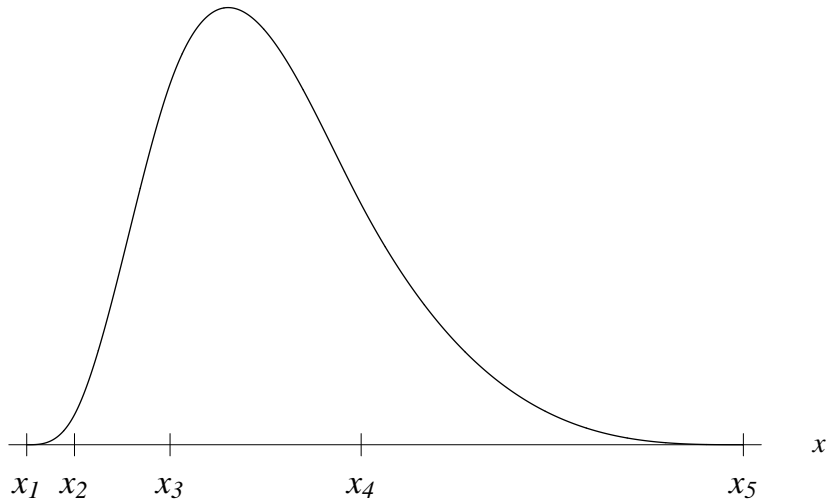


Figure 3.4: The non-uniform cubic B -spline $B(x)$ defined in Eq. (3.11) for $h_1 = x_2 - x_1 = 1/4$, $h_2 = x_3 - x_2 = 1/2$, $h_3 = x_4 - x_3 = 1$, and $h_4 = x_5 - x_4 = 2$.

splines would in general not be a B -spline curve. They could be oscillatory or not always positive valued. This would result in numerical instabilities in eigenvalue calculations. Our experience has shown that the best stable results are obtained when expanding the spline in terms of overlapping B -splines of the same kind and determining the expansion coefficients by matching the boundary conditions. For example, suppose that the unknown wave function is expanded in terms of cubic B -splines in the region $x \geq 0$, and it is needed to impose non-homogeneous boundary conditions for the wave function at $x = 0$. The modified spline $\tilde{B}(x)$ is expanded in terms of cubic B -splines to satisfy these criteria as,

$$\tilde{B}(x) = c_1 B(x+1) + c_2 B(x+2) + c_3 B(x+3) \quad \text{for } x \geq 0. \quad (3.12)$$

The terms in the region $x < 0$ are discarded. The unknown constants c_{1-3} are determined by the boundary conditions at $x = 0$, and the normalization

condition. Since there are three unknown constants and one normalization condition, only two boundary conditions can be imposed. It should be noted that the normalization condition also determines the shape of the spline. It is chosen to make the spline always positive and non-oscillatory. After the spline $\tilde{B}(x)$ is constructed, it is added to the wavefunction expansion given in Eq. (3.2) as,

$$\varphi(x) = \tilde{B}(x) + \sum_{i=2}^N \alpha_i B_i(x). \quad (3.13)$$

It should be noted that if the wavefunction is expanded in terms of B -splines, the wavefunction expansion given in Eq. (3.2) satisfies the homogeneous boundary conditions whereas the one given in Eq. (3.13) is for arbitrary boundary conditions at a given point.

3.5 Realization of the Self-Consistent Loop

Note that we have two coupled equations (Eqs. (2.27-2.28)) and the equilibrium conditions. Analytical methods for the solution do not exist and the separation of the equations is not possible for the penetration of the wavefunction into the barrier. The self-consistent loop can be established as follows. Firstly, Schrödinger equation is solved with the given n_i 's. Eigenfunctions and eigenenergies are calculated. This solution does not include electron-electron interaction. Secondly, these functionals are inserted into Poisson's equation and the equilibrium conditions. New $\phi_{sc}(x)$ including many body effects are obtained consistent with the equilibrium conditions. Then solutions are re-injected into Schrödinger

equation and this continues until convergence is achieved.

3.5.1 The Details of the Self Consistent Loop

Our aim is to solve Eq. (2.17) and Eq. (2.18) self consistently using auxiliary conditions Eqs. (2.19-2.21). The doping profile Eq. (2.21) of the structure must be given by the manufacturer. In other words, N_A , N_d , $N_{b,A}$, and n_e ,

$$n_e = \sum_{i \text{ occupied}} n_i = \sum_{i=1}^N n_i \quad (3.14)$$

must be given. But, both n_i 's (the areal concentration of electrons in i 'th sub-band) and the number of occupied levels N are not known. The energy gap E_g ($E_g = E_c - E_v$) is approximately 1.42 eV for GaAs. By using the boundary conditions $\phi_A(0) = 0$ and $\phi_A(l_A) \approx E_g$, one can solve for l_A as,

$$l_A \approx \sqrt{\frac{\kappa E_g}{2 \pi e^2 N_A}}. \quad (3.15)$$

Then, the calculation of l_d is straitforward by using Eq. (2.28). Since l_A , l_d , $N_{b,A}$, N_d , N_A , ($N_{dep} = N_A * l_A$), and n_e are all known, $\phi_A(x)$ and $\phi_d(x)$ are also completely determined by Eq. (2.26) and Eq. (2.27), and they will be unchanged in the remainder of the calculations.

The electron-electron interaction term $\phi_{e-e}(x)$ satisfies,

$$\phi_{e-e}''(x) = \frac{e}{\kappa} \sum_{i=1}^N n_i \varphi_i^2(x). \quad (3.16)$$

Table 3.1: List of the parameters in self consistent loop.

Given parameters	$n_e, x, w, N_{b,A}, N_d, N_A, T$
After straitforward calculations (independent of iterations, fixed)	$N_{dep}, l_A, l_d, \phi_A(x), \phi_d(x), \phi_w(x)$
To be solved self consistently	$E_i, \varphi_i(x), \mu, n_i, N$

Eq. (3.16) must be integrated twice with suitable boundary conditions in order to obtain $\phi_{e-e}(x)$. Similar integration process is made in the previous chapter to obtain acceptor contribution term $\phi_A(x)$ which satisfies $\phi_A''(x) = \frac{e}{\kappa}N_A$, and donor contribution term $\phi_d(x)$ which satisfies $\phi_d''(x) = \frac{e}{\kappa}N_d$. Note that, $\phi_A(x)$, $\phi_d(x)$, and $\phi_w(x)$ are calculated only once and will not change in successive iterations, whereas, $\phi_{e-e}(x)$ will change in each iteration until convergence is reached.

Iteration 0: Assume a value of N and start with Eq. (2.17). Here, $\phi_{sc}^0(x)$ does not include $\phi_{e-e}(x)$ term. In other words, Eq. (2.17) is solved for $\phi_{e-e}(x) = 0$. After E_i^0 and $\varphi_i^0(x)$'s are obtained, one solves for n_i using Eq. (2.19) by a numerical method. Since sum of n_i (n_e) is known, μ^0 can be easily found by a simple program for a given T and using a set of values E_i^0 which are just calculated in iteration 0. Using them, one calculates a set of n_i^0 . Putting these n_i^0 's into Eq. (2.18) and integrating twice one obtains $\phi_{sc}^1(x)$ which will be used for the next iteration. In the integration process, we have boundary conditions $\phi_{e-e}(x=0) = 0$ and $\phi_{e-e}'(x \rightarrow \infty) = 0$. Remember that integration of N_A and N_d are already done to obtain $\phi_A(x)$ and $\phi_d(x)$, previously.

Iteration n : Eq. (2.17) is solved for the previously calculated $\phi_{sc}^{n-1}(x)$ by using μ^{n-1} , $\varphi_i^{n-1}(x)$ and n_i^{n-1} . Thus, a new set of E_i^n and $\varphi_i^n(x)$ are obtained.

Using these one may obtain μ^n and n_i^n . These yield $\phi_{sc}^n(x)$ which will be used in iteration $n + 1$. One repeats these steps till convergence is achieved. We have implemented the convergence in our software as finding the same μ^n and E_i values in successive iterations within a prescribed accuracy. That is to say, we terminate the loop at n 'th iteration if $|\mu^n - \mu^{n-1}| \leq \Delta\mu$ and $|E_i^n - E_i^{n-1}| \leq \Delta E$.

3.6 The Finite Difference Method

The FDM is the most important competitor of the SFM used in this study. FDM is based on approximation of the derivatives of the unknown function by finite-difference quotients at a set of finite discretization points. Schrödinger equation can be converted into a simple algebraic eigenproblem,

$$\mathbf{H}\alpha = E\alpha, \quad (3.17)$$

where \mathbf{H} is banded, real symmetric sparse matrix. The two most common finite-difference quotients are the simplest 3-points approximation,

$$\varphi''_i = \frac{\varphi_{i+1} - 2\varphi_i + \varphi_{i-1}}{h^2} + O(h^2), \quad (3.18)$$

and the 5-points *Richardson extrapolation*,

$$\varphi''_i = \frac{-\varphi_{i+2} + 16\varphi_{i+1} - 30\varphi_i + 16\varphi_{i-1} - \varphi_{i-2}}{12h^2} + O(h^4). \quad (3.19)$$

Here, h is the grid spacing and subscript i is the knot index. Every physical situation is unique, but general consensus is that the additional effort required

for the higher order approximations is usually not justified [89].

The major advantage of FDM is the resultant simple matrix eigenvalue equation Eq. (3.17), and the ease of the calculation of its matrix elements. But its computational accuracy is considerably poorer than the SFM for discontinuous confining potentials $V(x)$.

3.7 Solution of the Two-Dimensional Schrödinger Equation

The two-dimensional (2-D) Schrödinger equation is given by,

$$-\frac{1}{2m^*}\left(\frac{\partial^2}{\partial x^2} + \frac{\partial^2}{\partial y^2}\right) \varphi(x, y) + V(x, y) \varphi(x, y) = E \varphi(x, y), \quad (3.20)$$

where $V(x, y)$ is the general 2-D confining potential, and m^* is assumed to be the same in x and y directions.

The unknown wavefunction $\varphi(x, y)$ is expanded in terms of N 2-D basis functions $\mathfrak{B}_i(x, y)$,

$$\varphi(x, y) = \sum_{i=1}^N \alpha_i \mathfrak{B}_i(x, y), \quad (3.21)$$

and $\mathfrak{B}_i(x, y)$ is the product of two B -splines in x and y directions as,

$$\mathfrak{B}_i(x, y) = B_i(x)B_i(y). \quad (3.22)$$

Here, each $\mathfrak{B}_i(x, y)$ is centered at a 2-D grid of points (x_i, y_i) . There are N_x and N_y ($N = N_x * N_y$) B -splines in x and y directions, respectively. The matrix elements of Eq. (3.3) are,

$$\begin{aligned}
H_{i,j} &= -\frac{1}{2m^*} \int B_i(x)B_j''(x)dx \int B_i(y)B_j(y)dy \\
&\quad -\frac{1}{2m^*} \int B_i(x)B_j(x)dx \int B_i(y)B_j''(y)dy \\
&\quad + \int \int B_i(x)B_i(y)V(x,y)B_j(x)B_j(y)dx dy, \\
S_{i,j} &= \int B_i(x)B_j(x)dx \int B_i(y)B_j(y)dy
\end{aligned} \tag{3.23}$$

The **H** and **S** matrices are sparse and real symmetric as in the 1-D Schrödinger equation case but their structure now depends on grid ordering (or numbering) since we have a 2-D mesh. As an illustrative example, sparsity of these matrices for cubic *B*-splines is shown in Fig. 3.5 and Fig. 3.6 for two different grid orderings given in Table 3.2.

Table 3.2: The grid ordering of 2-D mesh given in Fig. 3.5 and Fig. 3.6. The columns and rows in the tables correspond to N_x and N_y basis functions in x and y directions respectively.

Grid ordering in Fig. 3.5								Grid ordering in Fig. 3.6							
1	2	3	4	5	6	7	8	1	2	3	4	5	6	7	8
9	10	11	12	13	14	15	16	16	15	14	13	12	11	10	9
17	18	19	20	21	22	23	24	17	18	19	20	21	22	23	24
25	26	27	28	29	30	31	32	32	31	30	29	28	27	26	25
33	34	35	36	37	38	39	40	33	34	35	36	37	38	39	40
41	42	43	44	45	46	47	48	48	47	46	45	44	43	42	41
49	50	51	52	53	54	55	56	49	50	51	52	53	54	55	56
57	58	59	60	61	62	63	64	64	63	62	61	60	59	58	57

3.8 Solution of the Three-Dimensional Schrödinger Equation

For the 3-D Schrödinger equation,

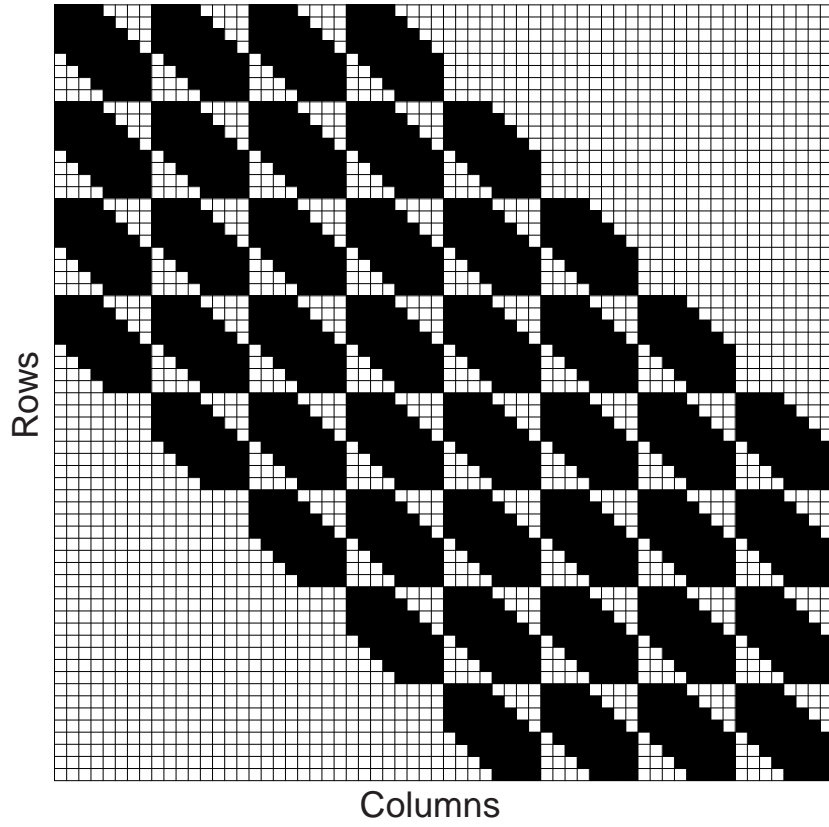


Figure 3.5: The \mathbf{H} or \mathbf{S} matrix elements of 8x8 mesh ($N = 64$). Non-zero matrix elements are shown by shaded boxes. In each row, the 2-D grid points are ordered from left to right.

$$-\frac{1}{2m^*} \left(\frac{\partial^2}{\partial x^2} + \frac{\partial^2}{\partial y^2} + \frac{\partial^2}{\partial z^2} \right) \varphi(x, y, z) + V(x, y, z) \varphi(x, y, z) = E \varphi(x, y, z), \quad (3.24)$$

The unknown wavefunction $\varphi(x, y, z)$ is expanded in terms of N 3-D basis functions $\mathfrak{B}_i(x, y, z)$,

$$\varphi(x, y, z) = \sum_{i=1}^N \alpha_i \mathfrak{B}_i(x, y, z), \quad (3.25)$$

such that $\mathfrak{B}_i(x, y, z)$ is the product of three B -splines in x , y , and z directions as,

$$\mathfrak{B}_i(x, y, z) = B_i(x)B_i(y)B_i(z). \quad (3.26)$$

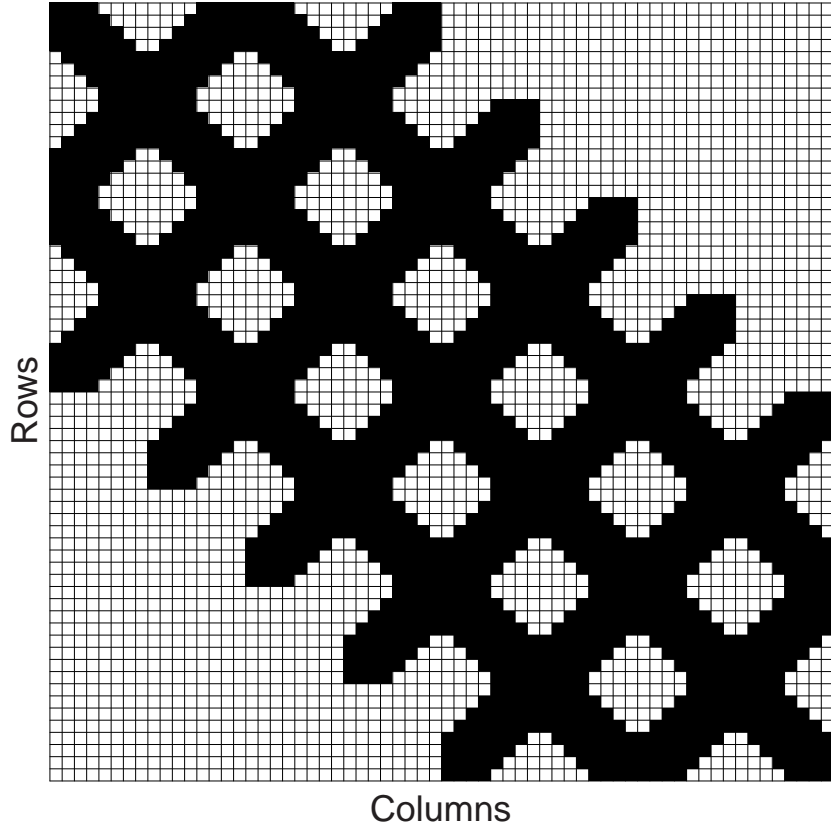


Figure 3.6: The \mathbf{H} or \mathbf{S} matrix elements of 8x8 mesh ($N = 64$). Non-zero matrix elements are shown by shaded boxes. In each row, the 2-D grid points are ordered from left to right and right to left in subsequent rows alternatively.

These 3-D basis functions are centered at the points (x_i, y_i, z_i) in a 3-D mesh.

The \mathbf{H} and \mathbf{S} matrix elements are

$$\begin{aligned}
H_{i,j} = & -\frac{1}{2m^*} \int B_i(x)B_j''(x)dx \int B_i(y)B_j(y)dy \int B_i(z)B_j(z)dz \\
& -\frac{1}{2m^*} \int B_i(x)B_j(x)dx \int B_i(y)B_j''(y)dy \int B_i(z)B_j(z)dz \\
& -\frac{1}{2m^*} \int B_i(x)B_j(x)dx \int B_i(y)B_j(y)dy \int B_i(z)B_j''(z)dz \quad . \quad (3.27) \\
& + \int \int B_i(x)B_i(y)B_i(z)V(x, y, z)B_j(x)B_j(y)B_j(z)dx dy dz \\
S_{i,j} = & \int B_i(x)B_j(x)dx \int B_i(y)B_j(y)dy \int B_i(z)B_j(z)dz
\end{aligned}$$

These matrices are sparse and real symmetric as in the 1-D or 2-D case but

like the 2-D case their structure is grid ordering dependent.

We now turn to a discussion of the results obtained by applying the SFM to the problems discussed in this chapter.

CHAPTER 4

THE RESULTS

In this chapter, computed results using SFM are given and compared with the available exact solutions and with the results of other numerical approaches. The calculations are performed by using a 2.5 GHz single CPU personal computer with 256 MB physical memory.

4.1 The Effect of B -Spline Order on the Results

There is a trade off between the efficiency of higher order B -splines and the resultant matrix complexity. The higher order splines give more accurate results for the same number of basis functions but since the bandwidth of resultant matrix dimensions and the order of polynomials in the integrals increase, more computational effort is needed. The efficiency of order of splines is problem dependent. For instance, we observed ten times greater efficiency of B -splines of order two compared to B -splines of order seven for continuous smooth confining potentials (see Section 4.2). But this is in general not the case for the discontinuous step-like potentials. The optimum results are obtained by using the cubic B -splines, and therefore they are used in the following sections.

4.2 The 1-D Harmonic Oscillator

In this section, simple 1-D harmonic oscillator described by Eq. (2.1) and Eq. (2.2) is solved using B -splines of different order k . The oscillator constant is our input parameter, and taken as $k_x = 1$. The basis splines are expanded in the region $x \in [-10, 10]$. The results are tabulated in Table 4.1.

Table 4.1: The five lowest eigenenergies (E_0 - E_4) of the 1-D harmonic oscillator with $k_x = 1$. In each case $N = 30$ basis functions are used and splines are expanded between $x = -10$ and $x = 10$.

Spline order k	E_0	E_1	E_2	E_3	E_4
3	0.50027	1.50201	2.50765	3.52050	4.54425
4	0.50001	1.50012	2.50062	3.50225	4.50639
5	0.50000	1.50001	2.50006	3.50028	4.50100
6	0.50000	1.50000	2.50001	3.50004	4.50016
7	0.50000	1.50000	2.50000	3.50001	4.50003
8	0.50000	1.50000	2.50000	3.50000	4.50000
Exact	0.5	1.5	2.5	3.5	4.5

As it is seen from Table 4.1, the results are exact up to 5th decimal place for $k = 8$ whereas accuracy is considerably poorer for $k = 3$. Actually, one needs $N = 300$ basis functions for $k = 3$, $N = 90$ basis functions for $k = 4$, $N = 55$ basis functions for $k = 5$, $N = 45$ basis functions for $k = 6$, and $N = 35$ basis functions for $k = 7$ to achieve a similar accuracy for $k = 8$.

4.3 The 1-D Attractive δ Function Potential

In this section, a single singular potential described by Eq. (2.3) and Eq. (2.4) is given as an example. The most convenient approximate form of δ function

is given in Eq. (2.7), although satisfactory results are obtained for the other forms (see Eqs. (2.5)-2.6)) for sufficiently small ϵ . The results obtained for the approximate formula given in Eq. (2.7) are tabulated in Table 4.2.

Table 4.2: The bound state energy level of single $-10\delta(x)$ potential described in Eq. (2.7) for different ϵ values.

ϵ	E_0
1	-7.17621
1/10	-30.7481
1/100	-45.8742
1/1000	-49.5300
1/10000	-49.9632
1/100000	-49.9960
1/1000000	-49.9960
Exact	-50

Table 4.2 shows that further decrease in ϵ has no effect on numerical results, because of the resultant ill-conditioned matrices.

The SFM method is an integral based method, in other words resultant integrals are important rather than the potential itself. The δ potential can also be represented in terms of its integral property,

$$\int_{x_i}^{x_f} f(x)\delta(x - x_0)dx = \begin{cases} f(x_0) & \text{for } x_i < x < x_f \\ 0 & \text{otherwise} \end{cases} . \quad (4.1)$$

Since δ potential is extremely sharp and discontinuous non-uniform grid should be constructed for accurate and efficient results. For this purpose, four knots are closely placed at the center of the potential and others distributed evenly in the expansion region $x \in [-1, 1]$. The results are tabulated in Table 4.3, and the

bound state wavefunction is plotted in Fig. 4.1.

Table 4.3: The bound state energy level of single $-10\delta(x)$ potential described in Eq. (4.1) for a non-uniform mesh. The basis functions are expanded in the region $x \in [-1, 1]$ and four of the knots are taken closely at the vicinity of the origin. The other knots are evenly distributed in $x \in [-1, 1]$. The knot spacing at the center is $1/100000$ of the total length. Further decrease in this separation resulted in ill-conditioned matrices, and has no improvement on the results.

N	E_0
5	-48.5671
11	-49.9870
21	-49.9973
101	-49.9975
Exact	-50

As it is seen from Table 4.3, very accurate (0.02% error) results are obtained in the results even with $N = 11$ basis functions. This is an explicit efficiency of the SFM. Such a singular potential can not be treated by the FDM at least usual manner.

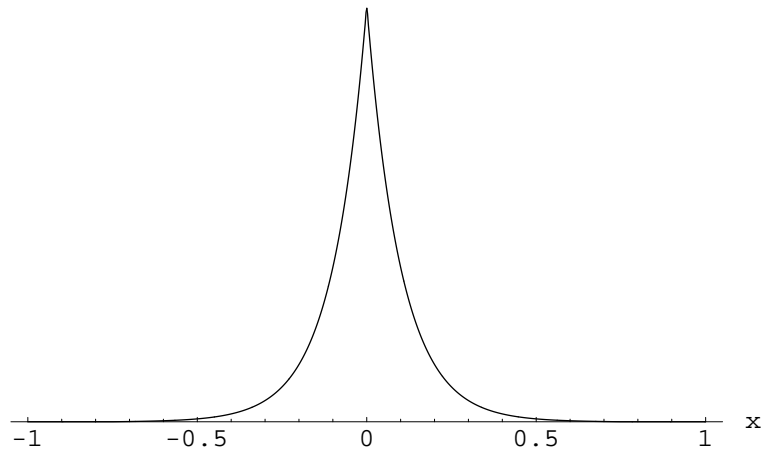


Figure 4.1: The bound state wavefunction of the singular potential $V(x) = -10\delta(x)$.

4.4 The 1-D Quantum Box

This is the simplest 1-D potential profile described by Eq. (2.8) and Eq. (2.31), but its solution requires satisfaction of boundary conditions at $x = 0$ and $x = L_x$ to achieve a great accuracy in SFM. The analytical solution involves $\sin(\cdot)$ or $\cos(\cdot)$ functions vanishing at the boundaries. But their first derivatives are not zero at the boundaries. This is not the case for B -splines. Their derivatives vanish at the boundaries. For the sake of simplicity, we take $L_x = \pi$ as the input parameter. The results are given in Table 4.4.

Table 4.4: The five lowest eigenenergies (E_1 - E_5) of the 1-D quantum box with $L_x = \pi$. The uniform grid cubic B -splines are used, and results are given for various number of basis functions N .

N	E_1	E_2	E_3	E_4	E_5
25	0.55054	2.20255	4.95717	8.81638	13.7830
100	0.51302	2.05209	4.61722	8.20845	12.8258
1000	0.50131	2.00526	4.51183	8.02103	12.5329
10,000	0.50013	2.00053	4.50118	8.00210	12.5033
100,000	0.50002	2.00006	4.50012	8.00021	12.5003
1,000,000	0.50000	2.00000	4.50001	8.00002	12.5000
Exact	0.5	2	4.5	8	12.5

As it is seen from Table 4.4, the accuracy is considerably poorer than the previous example, because, standard B -splines do not satisfy the boundary conditions of the wavefunction for the 1-D box. In the 1-D harmonic oscillator problem, the particle is penetrating into oscillator potential barrier and the wavefunction decays inside it. Thus, the wavefunction has vanishing first- and second-order

derivatives at the boundaries. The boundaries are determined by the expansion region of the splines. For higher order states, expansion region should be enlarged, since penetration length of the particle wavefunction increases. For the 1-D quantum box, on the other hand, the expansion region is fixed and the wavefunction has non-zero first order derivative at the boundaries. The following section describes how to handle this problem in SFM.

4.4.1 The 1-D Quantum Box Satisfying the Imposed Boundary Conditions

The unknown wavefunction is expanded in a similar manner as in Eq. (3.13). The only difference is the additional modified spline at $x = L_x$. This is an x axis reflected, symmetrical version of the $\tilde{B}(x)$ at $x = 0$. It is needed because the proper boundary conditions should also be satisfied at $x = L_x$. The expansion coefficients of $\tilde{B}(x)$ defined in Eq. (3.12) satisfying $\tilde{B}'(0) = 1$ are calculated as,

$$c_1 = 1, \quad c_2 = 0, \quad c_3 = -1 \quad . \quad (4.2)$$

The results are given in Table 4.5.

As it is seen from Table 4.5, striking improvement in the accuracy is obtained with splines satisfying proper boundary conditions. One needs more than 40,000 times more basis functions to achieve a similar accuracy with the case of standard splines.

Table 4.5: The five lowest eigenenergies (E_1 - E_5) of the 1-D quantum box with $L_x = \pi$. The splines are expanded between $x = 0$ and $x = L_x$, and the first and the last splines are modified by Eq.4.2 to satisfy proper boundary conditions supplied by ordinary B -splines at $x = 0$ and $x = L_x$. The uniform grid cubic B -splines are used, and results are given for various number of basis functions N .

N	E_1	E_2	E_3	E_4	E_5
5	0.50000	2.00014	4.50581	8.09581	13.2726
10	0.50000	2.00000	4.50008	8.00103	12.5080
25	0.50000	2.00000	4.50000	8.00000	12.5000
Exact	0.5	2	4.5	8	12.5

4.5 The 1-D Triangular Quantum Well

This type of confining potential which is described in Eq. (2.10) can be considered as a hybrid version of 1-D quantum harmonic oscillator and 1-D quantum box potentials. The potential barrier is impenetrable at $x = 0$ and the particle penetrates the triangular wall for $x > 0$. The results are given in Table 4.6 for standard cubic B -splines which are expanded in the region $x \in [0, 10]$.

Table 4.6: The five lowest eigenenergies (E_1 - E_5) of the 1-D triangular quantum well for $k_x = 1$. The uniform grid cubic B -splines are expanded in the region $x \in [0, 10]$, and the results are given for various number of basis functions N .

N	E_1	E_2	E_3	E_4	E_5
25	2.09580	3.48841	4.62869	5.63658	6.55805
200	1.88817	3.27703	4.41410	5.41905	6.33770
1000	1.86231	3.25117	4.38823	5.39317	6.31182
10,000	1.85641	3.24527	4.38233	5.38727	6.30592
100,000	1.85582	3.24467	4.38174	5.38668	6.30533
300,000	1.85579	3.24464	4.38170	5.38664	6.30529
Exact	1.85576	3.24461	4.38167	5.38661	6.30526

As it is seen from Table 4.6, results are almost correct up to 5th decimal place

for $N = 300,000$. But, it needs a lot of computational effort. This low accuracy is caused by the improper boundary conditions at $x = 0$. The next section explains the proper treatment in SFM.

4.5.1 The 1-D Triangular Quantum Well Satisfying the Imposed Boundary Conditions

The analytical solution of 1-D triangular quantum well involves Airy functions. These functions have non-vanishing first- and vanishing second-order derivatives at $x = 0$. This is also satisfied by the same spline used in the previous section and defined by Eq. (3.12) and Eq. (4.2). The results using this spline are given in Table 4.7.

Table 4.7: The five lowest eigenenergies (E_1 - E_5) of the 1-D triangular quantum well ($k_x = 1$) for various number of basis functions N . The uniform grid cubic B -splines are expanded in the region $x \in [0, 10]$, and the first basis in the expansion is modified to match the proper boundary conditions.

N	E_1	E_2	E_3	E_4	E_5
25	1.85576	3.24463	4.38173	5.38674	6.30551
60	1.85576	3.24461	4.38167	5.38661	6.30526
Exact	1.85576	3.24461	4.38167	5.38661	6.30526

If Tables 4.7 and 4.6 are compared, one observes a striking accuracy resulting from the imposed boundary condition. Only one, the first basis function is modified by proper boundary conditions but accuracy is increased by at least 5,000 times!

4.6 The 1-D Symmetric Double Rectangular Quantum Well (SDRQW)

In this section, the multiresolution analysis, non-uniform mesh construction and imposed boundary conditions are applied to a very steep SDRQW which is defined in Eq. (2.11). All these treatments are performed within SFM. At the end of section, FDM method is also applied to the SDRQW, and results are compared with SFM. In this example, the input parameters are $A = \frac{23}{2}$, $a = \frac{1}{32}$, $b = 1$, and $V_b = -400$.

4.6.1 The Multiresolution Analysis

The property of compression ensures us a compact representation of the wavefunction. The results obtained by discarding the expansion coefficients below the threshold are given in Table 4.8. The threshold is 10^{-6} and determined by so as not to change the results in the fifth decimal place.

In Table 4.8, the resolution level n corresponds to the resolution scale in the multiscale expansion Eq. (3.9). Coarsest level scaling functions are at level $n = 0$, and higher order detail functions or wavelets lie at $n = 1, 2, \dots$. The sums in Eq. (3.9) over i are taken from minimum i to maximum i values which are given in Table 4.8. If all basis functions were included, the index i would run from 1 to $N^{(n)}$. Compression is a major advantage used in the multiresolution analysis. As it is seen from Table 4.8, instead of using 1433 basis functions, one can compactly represents the wave functions with only 139 basis functions. The

Table 4.8: The multiscale expansion details of Eq. (3.9)

Resolution level n	Min. i	Max. i	Number of basis elements above threshold	Number of basis elements $N^{(n)}$ in original expansion.
0	1	20	20	20
1	1	17	17	17
2	16	25	10	40
3	38	49	12	86
4	82	97	16	178
5	170	193	24	362
6	346	385	40	730
Total number of basis elements used			139	1433

resultant wavefunction at various scales are shown in Fig. 4.2.

The calculated eigenvalues using multiresolution analysis are given in Table 4.9. The results are compared with the ordinary single scale expansion used in Eq. (3.2) for the same number of total basis functions ($N = 139$).

Table 4.9: The results of multiscale expansion compared to the ordinary SFM

Energy level n	Multiresolution results	Error in %	Single resolution results	Error in %	Exact
0	-62.2224	0.27	-42.1352	32.47	-62.3953
1	-62.1652	0.36	-41.8971	32.85	-62.3928

As it is seen from Table 4.9, the multiresolution analysis results are considerably better than the ordinary single scale SFM. One needs more than $N = 1000$ basis functions to get similar results which approximately corresponds to the total

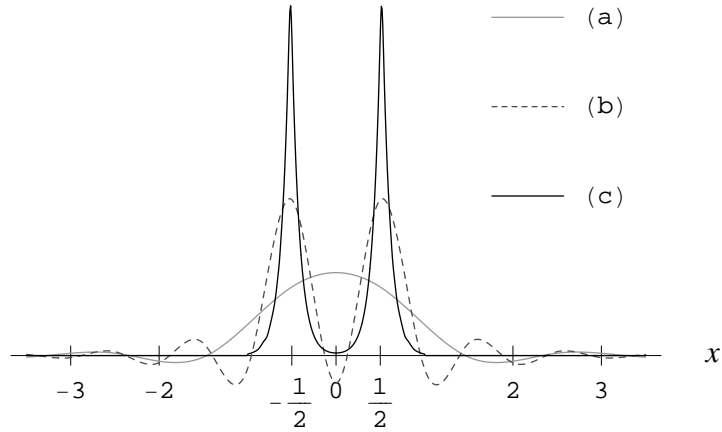


Figure 4.2: The wavefunction $\varphi(x)$ given in Eq. (3.9) is expanded up to various scales; (a) it is in the coarsest scale ($n = 0$), (b) it is expanded up to first detail scale ($n = 1$), and (c) it is expanded up to seventh detail scale ($n = 7$).

number of basis functions without compression in multiscale expansion.

4.6.2 The Non-Uniform Grid B -Splines

In this case, the same model problem is solved using single scale expansion Eq. (3.2) with non-uniform grid cubic B -splines. Denser knot spacing is taken in regions where there are rapid variations in the wavefunction. The distribution of the knots is summarized in Table 4.10. These knots define $N = 159$ non-uniform grid cubic B -spline basis functions and corresponding eigenenergies are compared with multiresolution calculations in Table 4.11. As it is clearly seen from Table 4.11, although slightly more basis functions need to be used in non-uniform grid calculations, a striking efficiency is obtained compared to multiresolution results. For a similar accuracy, one needs around $N = 15,000$ basis functions in ordinary uniform grid cubic B -spline expansion.

Table 4.10: The knot spacing for non-uniform cubic B -Splines

Number of knots	The region where the knots are taken	The region's description
1	$-\frac{23}{2} \leq x < -\frac{3}{2}$	Far from the first well
20	$-\frac{3}{2} \leq x < -\frac{1}{2} - \frac{1}{32}$	Close to the first well
50	$-\frac{1}{2} - \frac{1}{32} \leq x < -\frac{1}{2}$	Across the first well
20	$-\frac{1}{2} \leq x < \frac{1}{2}$	Between the wells
50	$\frac{1}{2} \leq x < \frac{1}{2} + \frac{1}{32}$	Across the second well
20	$\frac{1}{2} + \frac{1}{32} \leq x < \frac{3}{2}$	Close to the second well
1	$\frac{3}{2} \leq x < \frac{23}{2}$	Far from the second well

Table 4.11: The results of non-uniform grid cubic B -splines for $N = 159$ compared to multiresolution calculations for $N = 139$.

Energy level n	Multiresolution results	Error in %	Non-uniform grid results	Error in %	Exact
0	-62.2224	0.27	-62.3953	0.00	-62.3953
1	-62.1652	0.36	-62.3928	0.00	-62.3928

4.6.3 A More Compact Representation: Non-Uniform Grid B -Splines Satisfying the Imposed Boundary Conditions

In the previous examples, the symmetry of the model problem is not exploited and the basis functions are expanded in the full region $x \in [-\frac{23}{2}, \frac{23}{2}]$. In fact this is redundant for a symmetric problem, and approximately half number of the basis functions can be used in half of the expansion region $x \in [0, \frac{23}{2}]$ with the wavefunction $\varphi(x)$ satisfying the following boundary conditions,

$$\begin{aligned}
\varphi'(x) &= 0 \quad \text{for even solutions} \\
\varphi(x) &= 0 \quad \text{for odd solutions}
\end{aligned}
\tag{4.3}$$

Since we have only one imposed boundary condition for even or odd parity solutions, quadratic B -splines can in principle be used as a basis set. But our experience has shown that their accuracy is considerably poorer than the cubic B -splines for this particular model problem. The number of required quadratic B -spline basis functions is at least three times that of the required cubic B -spline basis for a similar accuracy. But higher order B -splines have resulted in no significant improvement. For these reasons, the optimum cubic B -spline basis set is used, and the other boundary conditions at $x = 0$ should be determined for maximum efficiency. The trivial boundary conditions are given in Eq. (4.3), and the rest are unknown. It is known that the exact wavefunction in the vicinity of origin ($-b \leq x \leq b$) without normalization has the form,

$$\begin{aligned}
\varphi(x) &= e^{k_b x} + e^{-k_b x} \quad \text{for even parity} \\
\varphi(x) &= e^{k_b x} - e^{-k_b x} \quad \text{for odd parity}
\end{aligned}
, \tag{4.4}$$

where k_b is the real positive wavevector. The resultant boundary conditions at $x = 0$ are therefore,

$$\begin{aligned}
\varphi(0) = 2, \quad \varphi'(0) = 0, \quad & \text{for even parity} \\
\varphi(0) = 0, \quad \varphi'(0) = 2k_b, \quad & \text{for odd parity}
\end{aligned} \tag{4.5}$$

Since relative magnitudes of the boundary conditions are important for the basis set (absolute magnitudes are scaled by the expansion coefficients), one should construct the basis splines satisfying,

$$\begin{aligned}
\tilde{B}(0) = 1, \quad \tilde{B}'(0) = 0, \quad & \text{for even parity} \\
\tilde{B}(0) = 0, \quad \tilde{B}'(0) = 1, \quad & \text{for odd parity}
\end{aligned} \tag{4.6}$$

The unknown wavefunction is expanded using Eq. (3.13), and the expansion coefficients of $\tilde{B}(x)$ as defined in Eq. (3.12) satisfying Eq. (4.6) are calculated as,

$$\begin{aligned}
c_1 = 1 \quad c_2 = 1 \quad c_3 = 1 \quad & \text{for even parity} \\
c_1 = 3 \quad c_2 = -1 \quad c_3 = 1 \quad & \text{for odd parity}
\end{aligned} \tag{4.7}$$

The non uniform mesh for $x \geq 0$ similar to the one given in Table 4.10 is constructed and described in Table 4.12. The calculated eigenvalues and their comparison to the non-uniform grid B -spline results are given in Table 4.13. It is shown that, although approximately a half the number of the basis functions are used compared that in the previous section, the same striking accuracy in the results are obtained.

Table 4.12: The knot spacing for non-uniform cubic B -splines satisfying imposed boundary conditions. This non-uniform mesh together with extra $\tilde{B}(x)$ spline defines $N = 85$ basis functions.

Number of knots	The region where the knots are taken	The region's description
6	$0 \leq x < \frac{1}{200}$	Between the wells, near the origin
10	$\frac{1}{200} \leq x < \frac{1}{2}$	Between the wells
50	$\frac{1}{2} \leq x < \frac{1}{2} + \frac{1}{32}$	Across the second well
20	$\frac{1}{2} + \frac{1}{32} \leq x < \frac{1}{2}$	Close to the second well
1	$\frac{3}{2} \leq x < \frac{23}{2}$	Far from the second well

Table 4.13: The results of non-uniform grid cubic B -splines satisfying imposed boundary conditions at $x = 0$ for $N = 85$ compared to non-uniform grid cubic B -splines calculations for $N = 159$. Note that error percentage is less than second decimal place.

Energy level n	Imposed boundary condition results	Error in %	Non-uniform grid results	Error in %	Exact
0	-62.3953	0.00	-62.3953	0.00	-62.3953
1	-62.3953	0.00	-62.3928	0.00	-62.3928

4.6.4 A Comparison with the FDM

The FDM is the most common method used in the related field of applications. The matrix bandwidths and the matrix structures are very similar to those in the SFM. The results are compared here. The model problem is solved with 3-points and 5-points FDM for various N . The results are tabulated in Table 4.14.

The model problem given in this study is a challenging problem for the FDM and the SFM. The confining potential is extremely sharp, rapidly varying and

Table 4.14: Three points and five points FDM results are compared with the SFM calculations for various N . Here N is the number of grid points in FDM and the number of basis functions in the SFM. The exact energies are $E_0 = -62.3953$, and $E_1 = -62.3928$

Three points FDM results	Error in %	Five points FDM results	Error in %	SFM results	Error in %
For $N = 1,000$					
$E_0 = -41.7814$	33.0	$E_0 = -39.7617$	36.2	$E_0 = -62.3266$	0.11
$E_1 = -41.7682$	33.1	$E_1 = -39.7460$	36.3	$E_1 = -62.3241$	0.11
For $N = 5,000$					
$E_0 = -65.6926$	-5.28	$E_0 = -65.5688$	-5.09	$E_0 = -62.3928$	0.00
$E_1 = -65.6907$	-5.30	$E_1 = -65.5669$	-5.09	$E_1 = -62.3902$	0.00
For $N = 10,000$					
$E_0 = -65.5098$	-4.99	$E_0 = -65.4785$	-4.94	$E_0 = -62.3951$	0.00
$E_1 = -65.5078$	-4.99	$E_1 = -65.4765$	-4.94	$E_1 = -62.3926$	0.00
For $N = 15,000$					
$E_0 = -60.5475$	2.96	$E_0 = -60.5342$	2.98	$E_0 = -62.3953$	0.00
$E_1 = -60.5446$	2.96	$E_1 = -60.5313$	2.98	$E_1 = -62.3928$	0.00

discontinuous. Since the FDM is a point based method, it can not properly resolve the sharp variations in the potential and thus convergence is not obtained even for $N = 10,000,000$. Moreover in the FDM, computed eigenvalues are above or below the exact values (see Table 4.14) depending on the localization of grids. On the other hand, the SFM is a "complete" method, it is based on the integrals or averaged values instead of the values at points, and thus is much more accurate in discontinuous or rapidly varying potentials.

4.7 The Asymmetric Double Rectangular Quantum Well (ADRQW)

The ADRQW confining potential is defined in Eq. (2.3). The input well parameters are taken as; $V_{b,1} = 10$, $V_{b,2} = 15$, $b_1 = b_2 = 1$, $a_1 = 1$ and $a_2 = 2$. There are six bound states for this configuration. The results obtained by uniform grid B -splines are given in Table 4.15.

Table 4.15: The six bound eigenenergies (E_1 - E_6) of the 1-D asymmetric double rectangular well potential with $V_{b,1} = 10$, $V_{b,2} = 15$, $b_1 = b_2 = 1$, $a_1 = 1$ and $a_2 = 2$. The uniform grid cubic B -splines are expanded in the region $x \in [-7, 7]$, and the results are given for various number of basis functions N .

N	E_1	E_2	E_3	E_4	E_5	E_6
50	-14.1188	-11.5103	-7.69602	-7.31163	-1.99468	-1.82281
100	-14.1201	-11.5164	-7.70316	-7.32942	-2.04141	-1.85342
500	-14.1206	-11.5181	-7.70500	-7.33301	-2.04656	-1.85817
1000	-14.1206	-11.5181	-7.70501	-7.33303	-2.04659	-1.85818
Exact	-14.1206	-11.5181	-7.70501	-7.33303	-2.04659	-1.85818

The high accuracy of the method is seen in Table 4.15. Even with $N = 50$ basis, the obtained results are acceptable.

4.8 The Double Quantum Well with Softened Coulomb Attraction

In this section, a double well potential with softened Coulomb attraction given in Ref. [85] and defined in Eq. 2.13 for $a = 0.1$ is studied. The results of the usual uniform grid approach is tabulated in Table 4.16.

Table 4.16: The six lowest eigenenergies (E_1 - E_6) of the 1-D double well potential with softened Coulomb attraction. The uniform grid cubic B -splines are expanded in the region $x \in [-25, 25]$, and the results are given for various number of basis functions N .

N	E_1	E_2	E_3	E_4	E_5	E_6
50	-5.2794	-3.66963	-.768295	-.589061	-.287179	-.243618
100	-5.34954	-3.75738	-.833229	-.596808	-.306564	-.245698
500	-5.53656	-3.90362	-.83649	-.606572	-.306979	-.248259
1000	-5.53663	-3.90371	-.836491	-.606576	-.306979	-.248260
Exact	-5.53663	-3.90371	-.836490	-.606576	-.306979	-.248260

The confining potential is smooth and shallow on most of the space, and the use of uniform grid is a waste of computational effort. Instead, more knots should be used in the places where potential changes rapidly. In the following section, non-uniform grid treatment is used for efficient calculations.

4.8.1 Non-Uniform Grid Treatment of the Double Quantum Well with Softened Coulomb Attraction

Since the potential given in Eq. 2.13 exhibits a smooth variation except in the vicinity of the points $x = \pm 1/2$, a special non-uniform mesh is used to increase the computational efficiency as given in Table 4.17. Table 4.17 is constructed to make density of the knots proportional to the slope of the confining potential,

and a more convenient mesh could probably be found. The results using this mesh is given in Table 4.18.

Table 4.17: Non-uniform grid mesh description of the double well potential with softened Coulomb attraction. Splines are expanded in the region $x \in [-25, 25]$, and total number of basis functions $N = 121$.

Number of knots	The region where the knots are taken
23	$-25 \leq x < -2$
10	$-2 \leq x < -1$
4	$-1 \leq x < -\frac{3}{4}$
20	$-\frac{3}{4} \leq x < -\frac{1}{4}$
10	$-\frac{1}{4} \leq x < \frac{1}{4}$
20	$\frac{1}{4} \leq x < \frac{3}{4}$
4	$\frac{3}{4} \leq x < 1$
10	$1 \leq x < 2$
23	$2 \leq x < 25$

Table 4.18: The six lowest eigenenergies (E_1 - E_6) of the 1-D double well potential with softened Coulomb attraction. The non-uniform grid mesh given in Table 4.17 is used.

N	E_1	E_2	E_3	E_4	E_5	E_6
121	-5.53663	-3.90371	-0.836491	-0.606576	-0.306979	-0.248260
Exact	-5.53663	-3.90371	-0.836490	-0.606576	-0.306979	-0.248260

As it is seen from Table 4.18, the non-uniform grid mesh requires approximately five times less basis functions for a similar accuracy compared with the ordinary uniform mesh. The actual efficiency is mesh and problem dependent. For sharper potential profiles, efficiency of non-uniform grid mesh is more apparent.

4.9 Self-Consistent Calculations

In this section, unless otherwise is stated all energies are in meV, all length units are in micrometer (μm), all mass units are in the electron unit mass, and all charge units are in the electron unit charge e . During the calculations, it is chosen as $\Delta\mu = \Delta E = 0.01\text{meV}$ for being the convergence criteria.

The first example is taken from [40]. It is an AlGaAs-GaAs heterojunction. The given parameters are: $n_e = 5000/\mu\text{m}^2$, $V_b=300\text{meV}$, $N_d = 500000/\mu\text{m}^3$, $N_{dep} = 500/\mu\text{m}^2$, $N_A = 160/\mu\text{m}^3$, $w = 0$, $T = 300\text{K}$. The self consistent solution according to [40] is given in Table 4.19.

Table 4.19: Chemical potential and energy levels (meV) of [40].

μ	E1	E2	E3	E4	E5
38.1	55.3	87.9	107	120	130

But these values only approximately satisfy $ne = 5000/\mu\text{m}^2$ requirement. The conduction bandgap is approximately 1640 meV (E_g) at GaAs side. And at interface ($x = 0$) there is 300 meV barrier (V_b) at AlGaAs side. This triangular-like potential well can never have bound energy levels greater than V_b . It means that E_i can only be smaller than V_b . Indeed there are 19 bound levels for this example according to our calculations and they are given in Table 4.20.

$N = 100$ basis functions are used and convergence is achieved in 38 iterations. Total run-time is approximately 23 seconds for a standard PII-333 PC.

Table 4.20: Chemical potential and energy levels (meV) for Example 1, our calculations.

μ	E1	E2	E3	E4	E5	E6	E7	E8	E9
33.1	55	87	107	121	133	142	151	158	165
E10	E11	E12	E13	E14	E15	E16	E17	E18	E19
173	181	191	202	214	226	240	255	271	287

The second example is also an AlGaAs-GaAs heterojunction which is taken from the Bastard's work [41]. For this case, the parameters are: $n_e = 2000/\mu\text{m}^2$, $V_b=318\text{meV}$, $N_d = 0/\mu\text{m}^3$, $N_{dep} = 400/\mu\text{m}^2$, $N_A = 100/\mu\text{m}^3$, $w = 0$. Since n_e is given and $N = 1$ (electronic quantum limit), $T = 0$. Table 4.21 shows a comparison of [41] with our calculations.

Table 4.21: First bound energy level with various n_e

n_e	$2000/\mu\text{m}^2$	$4000/\mu\text{m}^2$	$6000/\mu\text{m}^2$	$8000/\mu\text{m}^2$	$10000/\mu\text{m}^2$
E1(Bastard's)	32.00	45.60	56.71	66.30	74.68
E1(ours)	32.72	46.45	57.65	67.30	75.83

Some expectation values that are compared with the Bastard's results [41] are summarized in Table 4.22 with $n_e = 6000/\mu\text{m}^2$.

Table 4.22: Some expectation values for the second example, $n_e = 6000/\mu\text{m}^2$

	$\langle -e\phi_{sc}(x)U(x) \rangle$	$\langle -e\phi_{sc}(x)U(-x) \rangle$	$\langle VbU(-x) \rangle$
Bastard's [41]	37.76 meV	-0.092 meV	4.86 meV
Ours	42.55 meV	-0.062 meV	3.49 meV
	$\langle U(-x) \rangle$	$\langle x \rangle$	$\langle -e\phi_A(x) \rangle$
Bastard's [41]	1.53 %	72.43 A	3.44 meV
Ours	1.10 %	67.50 A	4.38 meV

The third example is taken from [42]. It is an GaAs/Al_xGa_{1-x}As heterojunction with parameters given below. The electric quantum limit is assumed. The results are given in Table 4.23.

Table 4.23: The results of the self-consistent calculation for the third example; $V_b = 300\text{meV}$, and $\kappa = 13$.

n_e	N_{dep}	N_A	$E_1\text{Ref [42]}$	$E_1\text{Ours}$
$5000/\mu\text{m}^2$	$460/\mu\text{m}^2$	$100/\mu\text{m}^2$	51.9 meV	52.79 meV
$4000/\mu\text{m}^2$	$4.6/\mu\text{m}^2$	$0.01/\mu\text{m}^2$	43.0 meV	43.41 meV
$4000/\mu\text{m}^2$	$1380/\mu\text{m}^2$	$900/\mu\text{m}^2$	50.5 meV	53.90 meV

The fourth example and its results are given in Table 4.24. It is a two level system. Again, it is a GaAs/Al_xGa_{1-x}As heterojunction. The results are compared with [43].

Table 4.24: The results of the self-consistent calculation for the fourth example; $V_b = 300\text{meV}$, $\kappa = 13$, $N_{dep} = 800/\mu\text{m}^2$, and $N_A = 300/\mu\text{m}^2$.

n_e	$E_1\text{Ref [43]}$	$E_1\text{Ours}$	$E_2\text{Ref [43]}$	$E_2\text{Ours}$
$1000/\mu\text{m}^2$	28.47 meV	28.58 meV	45.66 meV	45.74 meV
$5000/\mu\text{m}^2$	54.56 meV	55.18 meV	77.20 meV	77.79 meV

4.10 Two-Dimensional Case

In this section, striking efficiency of SFM is shown by two examples; 2-D harmonic oscillator and a 2-D quantum box. The numerical results are compared with the exact solutions.

4.10.1 The 2-D Harmonic Oscillator

The 2-D harmonic oscillator potential is described by Eq. (2.30) and Eq. (2.31). The numerical results for the input parameters $k_x = 1$, and $k_y = 1.21$ compared with the exact values for different number of basis functions are given in Table 4.25 and a few wavefunctions are plotted in Figs. 4.3-4.6. The basis functions are expanded in a 2-D uniform mesh defined by $x \in [-9/2, 9/2]$ and $y \in [-9/2, 9/2]$.

Table 4.25: The SFM results for 2-D harmonic oscillator with $k_x = 1$, and $k_y = 1.21$ compared with the exact values.

Energy level	SFM with $N_x = 10$, $N_y = 10$ ($N = 100$).	SFM with $N_x = 20$, $N_y = 20$ ($N = 400$).	Exact
$n_x = 0, n_y = 0$	1.05008	1.05000	1.05
$n_x = 1, n_y = 0$	2.05039	2.05000	2.05
$n_x = 0, n_y = 1$	2.15058	2.15000	2.15
$n_x = 2, n_y = 0$	3.05191	3.05000	3.05
$n_x = 1, n_y = 1$	3.15088	3.15000	3.15

The confining potential in Table 4.25 is a smooth potential. Thus, very accurate results can be obtained by using an ordinary uniform mesh and a few number of basis functions. This is a typical aspect of the method, and valid in general for all continuous and smooth confining potentials.

4.10.2 The 2-D Quantum Box

We have a 2-D quantum box described by Eq. (2.32) and Eq. (2.33). The input parameters are the box dimensions; $L_x = \pi$ and $L_y = \pi/\sqrt{2}$. At the box

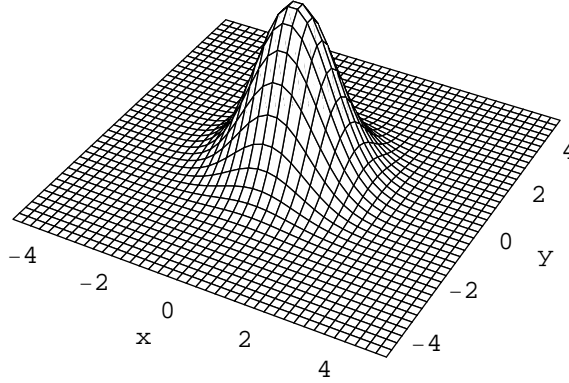


Figure 4.3: The wavefunction for the 2-D harmonic oscillator potential; $k_x = 1$, $k_y = 1.21$, $n_x = 0$, $n_y = 0$, $N_x = 10$, and $N_y = 10$

boundaries, the B -splines described by Eq. (3.12) and Eq. 4.2 are used to satisfy proper boundary conditions. The basis functions cover the region $x \in [0, L_x]$, $y \in [0, L_y]$, and the results are tabulated in Table 4.26.

Table 4.26: The SFM results of 2-D quantum box of dimensions $L_x = \pi$ and $L_y = \pi/\sqrt{2}$ compared with the exact values. The proper B -splines are used at the box surface to satisfy the imposed boundary conditions.

Energy level	SFM with $N_x = 10$, $N_y = 7$ ($N = 70$).	SFM with $N_x = 20$, $N_y = 15$ ($N = 300$).	Exact
$n_x = 1, n_y = 1$	1.50000	1.50000	1.5
$n_x = 2, n_y = 1$	3.00000	3.00000	3
$n_x = 1, n_y = 2$	4.50004	4.50000	4.5
$n_x = 3, n_y = 1$	5.50008	5.50000	5.5
$n_x = 2, n_y = 2$	6.00004	6.00000	6

Table 4.26 shows the striking efficiency of SFM. Only with a few hundred

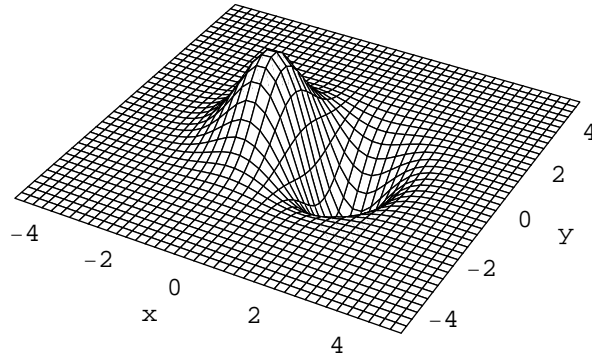


Figure 4.4: The wavefunction for the 2-D harmonic oscillator potential; $k_x = 1$, $k_y = 1.21$, $n_x = 1$, $n_y = 0$, $N_x = 10$, and $N_y = 10$

basis functions a 2-D problem is solved very accurately. If boundary conditions were not matched, it would require about a billion basis functions for a similar accuracy.

4.11 Three-Dimensional Case

In this section a 3-D harmonic oscillator and a 3-D quantum box (finite quantum wire) are examined. An attractive impurity potential is also added to the finite quantum wire and its effect on the energy levels and the wavefunctions are observed.

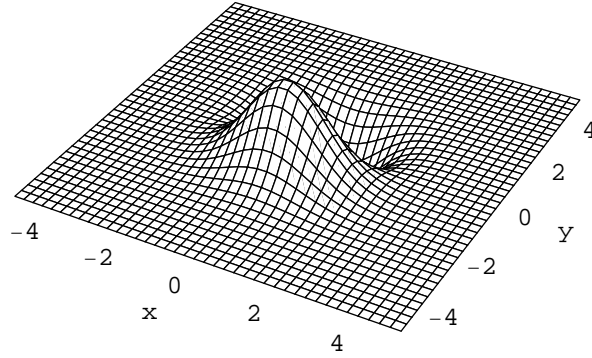


Figure 4.5: The wavefunction for the 2-D harmonic oscillator potential; $k_x = 1$, $k_y = 1.21$, $n_x = 0$, $n_y = 1$, $N_x = 10$, and $N_y = 10$

4.11.1 The 3-D Harmonic Oscillator

The 3-D harmonic oscillator potential is described by Eq. (2.34) and Eq. (2.35).

The numerical results for the input parameters $k_x = k_y = k_z = 1$ compared with the exact values are given in Table 4.27. The basis functions are expanded in a 3-D volume defined by $x \in [-9/2, 9/2]$, $y \in [-9/2, 9/2]$, and $z \in [-9/2, 9/2]$.

Table 4.27: The SFM results for 3-D harmonic oscillator for $k_x = k_y = k_z = 1$ compared with the exact values.

Energy level	SFM with $N_x = 10$, $N_y = 10$, and $N_z = 10$ ($N = 1000$).	Exact
$n_x = 0, n_y = 0, n_z = 0$	1.50000	1.5
$n_x = 1, n_y = 0, n_z = 0$	2.50022	2.5
$n_x = 0, n_y = 1, n_z = 0$	2.50022	2.5
$n_x = 0, n_y = 0, n_z = 1$	2.50022	2.5

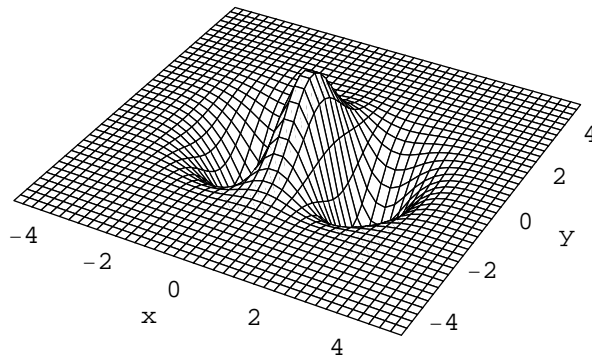


Figure 4.6: The wavefunction for the 2-D harmonic oscillator potential; $k_x = 1$, $k_y = 1.21$, $n_x = 2$, $n_y = 0$, $N_x = 10$, and $N_y = 10$

Since we have a continuous and smooth confining potential in Table 4.27, we obtained very accurate results as in the case of 2-D harmonic oscillator given in Table 4.25. Moreover, if these two tables compared, it is seen that accuracy in the results are better for 3-D harmonic oscillator if the number of the basis functions along each direction is considered. This is a general aspect and advantage of the method and also mentioned in the next section.

4.11.2 The 3-D Quantum Box (Finite Quantum Wire)

We have a 3-D quantum box described by Eq. (2.36) and Eq. (2.37). The input parameters are the box dimensions, $L_x = \pi$, $L_y = \pi/\sqrt{2}$ and $L_z = \pi/\sqrt{3}$. The B -splines described by Eq. (3.12) and Eq. 4.2 are used at the box boundaries to satisfy the proper boundary conditions. The basis functions cover the region

$x \in [0, L_x]$, $y \in [0, L_y]$, $z \in [0, L_z]$, and the results are tabulated in Table 4.28.

Table 4.28: The SFM results of 3-D quantum box of dimensions $L_x = \pi$, $L_y = \pi/\sqrt{2}$ and $L_z = \pi/\sqrt{3}$ compared with the exact values. The proper B -splines are used at the box surface to satisfy the imposed boundary conditions.

Energy level	SFM with $N_x = 5$, $N_y = 5$ and $N_z = 5$ ($N = 125$).	SFM with $N_x = 10$, $N_y = 10$ and $N_z = 10$ ($N = 1000$).	Exact
$n_x = 1, n_y = 1, n_z = 1$	3.00000	3.00000	3
$n_x = 2, n_y = 1, n_z = 1$	4.50014	4.50000	4.5
$n_x = 1, n_y = 2, n_z = 1$	6.00028	6.00000	6
$n_x = 3, n_y = 1, n_z = 1$	7.00581	7.00000	7
$n_x = 1, n_y = 1, n_z = 2$	7.50042	7.50000	7.5
$n_x = 2, n_y = 2, n_z = 1$	7.50042	7.50000	7.5

As it is shown in Table 4.28, very accurate results are obtained by using only ten basis functions along each direction. Moreover, if Table 4.28 and Table 4.5 are compared, it is seen that computational efficiency of the method is increased in the point of number of required functions along each direction. This is also the case for 2-D confining potentials (see Table 4.26). The total number of basis functions are exponentially proportional with the dimensionality of the confining potential, but hopefully one needs to use lesser number of basis functions along each direction. This is a great advantage of the SFM.

4.11.3 The Finite Quantum Wire with Attractive Impurity

In this section, a 3-D box shaped attractive impurity potential is added to the different locations of the finite quantum wire described in the previous section.

The impurity potential is defined by,

$$V_{imp}(x, y, z) = \begin{cases} -10 & \text{for } x, y \text{ and } z \in \Omega \\ 0 & \text{otherwise,} \end{cases} \quad (4.8)$$

where Ω is a 3-D box centered at the point (x_0, y_0, z_0) with dimensions l_x, l_y and l_z along x, y and z directions, respectively.

The impurity potential is taken in two different places. It is taken at $(L_x/2, L_y/2, L_z/2)$ and $(L_x/2 + 2L_x/30, L_y/2, L_z/2)$ as being the first and second examples, respectively. In both cases it is taken as $l_x = 2L_x/15, l_y = 2L_y/15, l_z = 2L_z/15$, and $N_x = N_y = N_z = 12$. The results are given in Table 4.29, and some sample wavefunctions are plotted in Figs. 4.7-4.9.

Table 4.29: The SFM results of finite quantum wire of dimensions $L_x = \pi, L_y = \pi/\sqrt{2}$ and $L_z = \pi/\sqrt{3}$. The proper B -splines are used at the box surface to satisfy the imposed boundary conditions. The impurity is taken at $(L_x/2, L_y/2, L_z/2)$ and $(L_x/2 + 2L_x/30, L_y/2, L_z/2)$ for the first and second examples, respectively. In both cases $l_x = 2L_x/15, l_y = 2L_y/15, l_z = 2L_z/15, N_x = N_y = N_z = 12$, and $N = 1728$.

Energy level	Example 1	Example 2	Exact values without impurity
$n_x = 1, n_y = 1, n_z = 1$	2.62224	2.67587	3
$n_x = 2, n_y = 1, n_z = 1$	4.47624	4.29645	4.5
$n_x = 1, n_y = 2, n_z = 1$	5.97708	5.98183	6
$n_x = 3, n_y = 1, n_z = 1$	6.69725	6.94527	7
$n_x = 1, n_y = 1, n_z = 2$	7.47746	7.48213	7.5
$n_x = 2, n_y = 2, n_z = 1$	7.49833	7.48496	7.5

Since exact solution of the problem is not available, we can not verify the accuracy of the results given in Table 4.29. But general accuracy of SFM on different problems reveals that these converged results supposed to be reliable.

It should be noted that in both examples, the degeneracy of the eigenvalues for the fourth and fifth excited states are removed with added impurity, although the added impurity in Example 1 is symmetric with respect to the finite quantum wire. But, this is not a common case for all types of degenerate states. The added attractive impurity is also lowered the energy levels in both examples, as expected. It should also be noted that orthogonality of the wavefunctions are apparent in Figs. 4.7-4.9. The ground state probability amplitude of the particle in Example 2 is shifted towards the attractive impurity as in Fig. 4.7, but it is weighted in the opposite side for the first excited state as in Fig. 4.8.

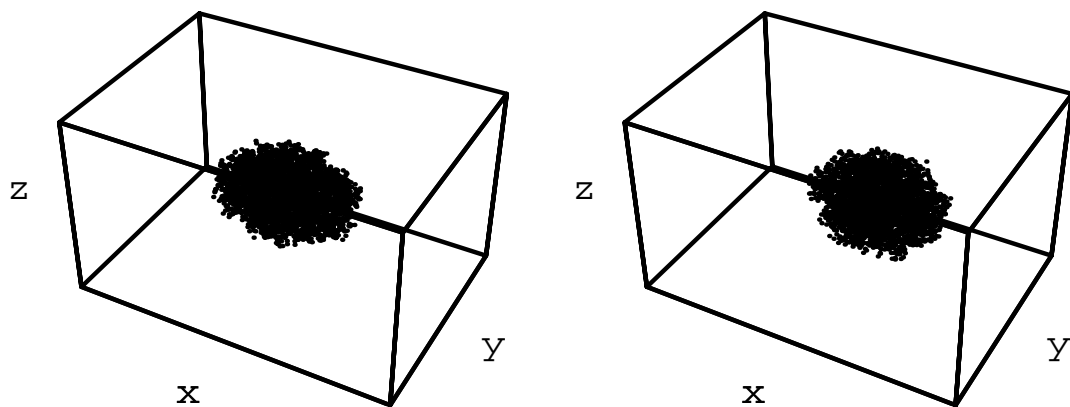


Figure 4.7: The ground state probability amplitude of the particle in the finite quantum wires (see Table 4.29). There is no impurity potential in the left-hand side plot, the right-hand side plot on the other hand is for Example 2.

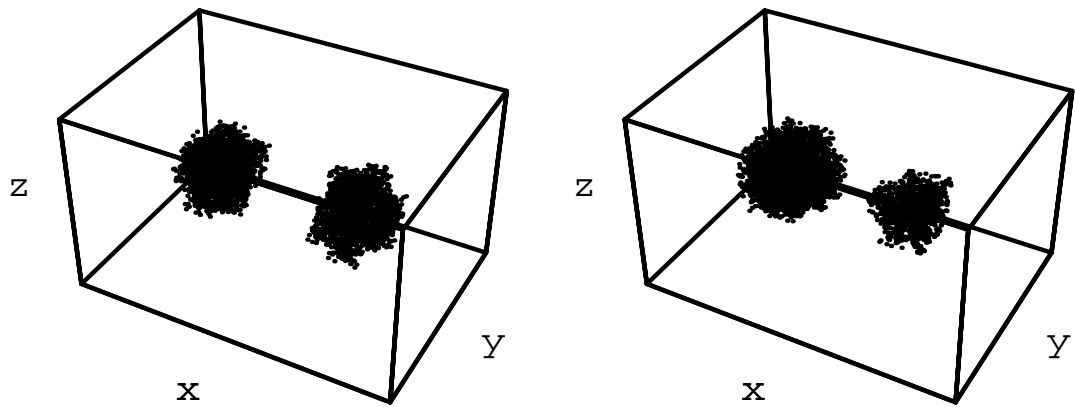


Figure 4.8: The first excited state probability amplitude of the particle in the finite quantum wires (see Table 4.29). There is no impurity potential in the left-hand side plot, the right-hand side plot on the other hand is for Example 2.

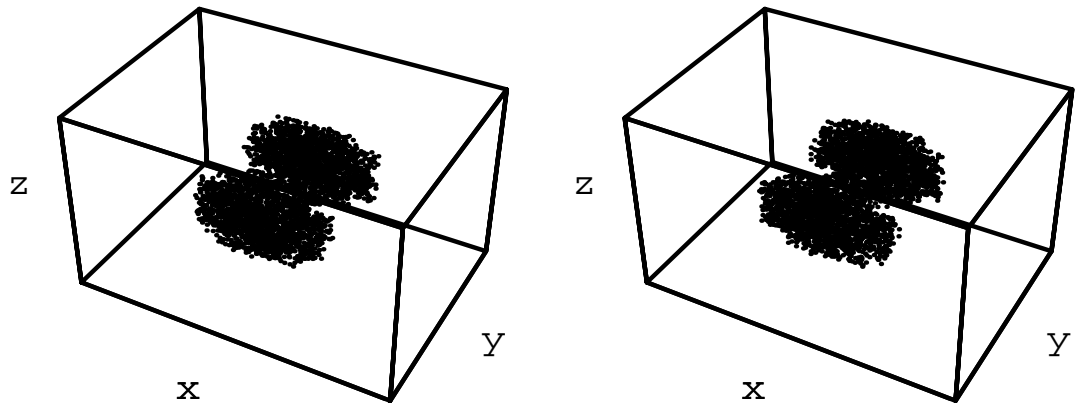


Figure 4.9: The second excited state probability amplitude of the particle in the finite quantum wires (see Table 4.29). There is no impurity potential in the left-hand side plot, the right-hand side plot on the other hand is for Example 2.

CHAPTER 5

CONCLUSION

In this thesis, we presented a numerical real space method (SFM) that is very effective for the electronic structure calculation of arbitrary confining potential. The SFM method is a basis function method. The basis functions if suitably chosen plays a very important role in the efficiency of the method. The *B*-splines proved their efficiency in the electronic structure calculations, and thus they are used in this study.

One of the important goals of any numerical method is to calculate accurate results with minimum computational effort. For our case, this corresponds to an accurate representation of the system with minimum number of basis functions. The MRA (or wavelet analysis) opens such a way by the concept of compression. The MRA is applied to the SFM and approximately seven times greater efficiency in the total number of basis functions are realized for the same accuracy in the cost of difficult implementation and increased matrix complexity. The SFM is very flexible and can be made thousands of times more accurate in proper treatments which include non-uniform grid expansion and imposed boundary conditions. For example, we have achieved a similar accuracy with 40,000 times less number of basis functions in a 1-D quantum box, and 5,000 times less number of basis

functions in a 1-D triangular well compared with ordinary uniform grid approach.

It is possible to increase the computational efficiency even further. These are the tricks to reduce the execution time. It is known that if the confining potential is analytically integrable, all the integrals in the matrix elements can be evaluated exactly in the form of integration tables once, before the matrix filling procedure. In such cases, no integration process takes places during the execution and this significantly improves the run-time.

In the cases of confining potentials which are not analytically integrable, a numerical integration process should take place during the run-time just for the term related with the confining potential. The other terms are fetched from the integration tables.

We have first written all the subroutines in Mathematica and Matlab. Then, it is ported to a mixture of C/Fortran programming language code and verified with the previous results of the two reliable mathematical package programs. The porting of the subroutines to C/Fortran code has two reasons. Firstly, since C/Fortran code is a compiled code but not an interpreter, it is almost 1000-3000 times faster in matrix filling process. Secondly, there is an invaluable mathematical library in Fortran for dedicated sparse algorithms of eigensystem calculations.

The SFM and the FDM method is most effective in 1-D confining potentials. One of the reasons for this fact is related with the resulting matrix dimensions which are exponentially proportional to the dimensionality of the confining potential. It is a great advantage of the SFM that one needs to use lesser number of

basis functions along each direction for 2-, and 3-D confining potentials compared to the 1-D case. This is not the case for the FDM, where obtaining a four digit accuracy in the results for a simple 3-D harmonic oscillator seems to be impossible [90]. The methods are also most efficient for 1-D confining potentials which results in the simplest matrix structures. For a non-periodic confining potential, both method results in banded, real symmetric matrices, but unfortunately this simple banded form is not maintained for the 2- or 3-D confining potentials. Dedicated matrix algorithms should be written for each particular case for a similar computational efficiency in the 1-D case.

The SFM is compared with the most common real space method FDM, and its superiority over FDM is explicitly shown in a steep SDRQW example. Although the FDM is the greatest competitor of the SFM in that area, its efficiency can only be comparable to SFM in 1-D continuous confining potentials. For higher dimensions or discontinuous potentials it fails to give accurate results. Because, it is a point based method and location of this points are sensitive for the results. The SFM on the other hand, is a complete method and based on the integrals or averaged values making it much more robust even in delta function potentials. Such potentials can not be solved by FDM, whereas SFM can obtain very accurate results just by using a few basis functions.

But, the FDM results in a simple matrix eigenvalue equation whereas one should solve a generalized matrix eigenvalue equation in the SFM because of the fact that B -splines are not orthogonal. Moreover, implementation and calculation

of the FDM matrix elements are easier.

One of the major weakness of both methods is seen on unlocalized or not well localized energy states. For such states, in principle, wavefunction penetration region extends unboundedly, which can not be handled by the finite domain basis function expansion method. The method may fail for such states. But these are only ideal mathematical cases. In practical device physics, particles can never penetrate unboundedly, and the method described in this work should give correct results for a reasonable practical penetration region which has usually a few wavelengths of depth.

The SFM inevitably puts infinite energy barriers at the boundaries of the expansion region, and as a result the energy levels are pulled up. This can also be considered as a drawback of the SFM. In the worst case, this may remove some of the shallow energy levels, resulting in a less number of bound states. Nevertheless the method used in this study is very powerful and efficient. Generally almost all the numerical results are consistent with the exact solutions with an error of far less than 1%. Moreover, this flexible and useful method can be applied to any arbitrary confining potential or geometry.

A variety of single electron confining potentials are solved using the SFM in 1-, 2- and 3-D. The efficiency and the accuracy of the method is explicitly shown on different types of confining potentials. These include, continuous, discontinuous, step and singular type of potentials. The SFM is found to be very powerful in all these potentials whereas the solution is either not available or very difficult

for the FDM in some cases. The flexibility of the method is also suitable not only for the single electron calculations but for the self consistent and many body calculations. This is explicitly shown for the self-consistent solution of Schrödinger's and Poisson's equations for a modulation doped heterojunction, and the results obtained are compared well with the previous works.

The order of the splines are important in the accuracy of the results. One of the contribution of this work is the investigation of the spline order effect on the resultant accuracy; as the spline order increases, one gets better accuracy in the cost of matrix complexity. We used B -splines of different order in the harmonic oscillator problem, and tested the resultant accuracy against the computational effort. It is shown that the optimal basis set is the cubic B -splines. Another contribution is a methodology on the construction of modified splines to satisfy imposed boundary conditions of the wavefunction in the SFM. Using such modified splines better accuracy is achieved. A further contribution is the first application of the MRA to the SFM in a condensed matter physics problem. The unknown wavefunction is resolved in all scales and the concept of compression is successfully achieved. An additional contribution is the solution of a finite quantum wire using the SFM for the first time. The finite quantum wire is first solved without any impurity, then an attractive impurity is added and its effects are investigated. The impurity is shown to remove the degeneracy and lower the energy levels as expected. The final contribution is made in the field of computational techniques. Very efficient algorithms for the SFM is written . These algorithms

exploit almost all the properties of the solution, and therefore are very effective and accurate. They make it possible to use $N = 1,000,000$ basis functions in 1-D problems within the SFM by using an ordinary personal computer. It is left as a future work to design such dedicated matrix algorithms for higher dimensional problems. It would then be possible to solve some 2- and 3-D problems with great accuracy, such as the coupled finite quantum wire problem.

In conclusion, finite basis sets based on B -splines have proved to be extremely useful in many low-dimensional physics calculations. We have given only a few possible examples just to show the effectiveness of this new method. We believe it can easily and effectively be applied to more complicated problems involving strong electron correlations. And, the method can easily be extended to momentum space to handle unlocalized states which is not proper for the real space methods.

REFERENCES

- [1] L. Esaki and R. Tsu, IBM Research Center Report No. RC2418, 1969 (unpublished).
- [2] Paul N. Butcher, Norman H. March, Mario P. Tosi, *Physics of Low-Dimensional Semiconductor Structures*, (Plenum Press, New York and London 1993).
- [3] Minko Balkanski and Nikolai Andreev, *Advanced Electronic Technologies and Systems Based on Low-Dimensional Quantum Devices*, (Kluwer Academic Publishers, Boston, 1997).
- [4] Keith Barnham and Dimitri Vvedensky, *Low-Dimensional Semiconductor Structures : Fundamentals and Device Applications*, (Cambridge University Press, New York, 2000).
- [5] Gunther Bauer, Friedemar Kuchar, Helmut Heinrich, eds., *Low-Dimensional Electronic Systems : New Concepts : Proceedings of the Seventh International Winter School, Mauterndorf, Austria, February 24-28, 1992*, (Springer-Verlag, New York, 1992).
- [6] Tobias Brandes, *Low-Dimensional Systems : Interactions and Transport Properties : Lectures of a Workshop Held in Hamburg, Germany, July 27-28, 1999*, (Springer, New York, 2000).
- [7] Lawrence Challis, *Electron-Phonon Interactions in Low-Dimensional Structures*, (Oxford University Press, New York, 2003).
- [8] John H. Davies, *The Physics of Low-Dimensional Semiconductors : An Introduction*, (Cambridge University Press, New York, 1998).
- [9] Karl Eberl, Pierre M. Petroff, and Piet Demeester, *Low-Dimensional Structures Prepared by Epitaxial Growth or Regrowth on Patterned Substrates*, (Kluwer Academic Publishers, Boston, 1995).
- [10] M.Jonson, T.Claeson, *Low-Dimensional Properties of Solids: Proceedings of the Nobel Jubilee Symposium Gothenburg, Sweden, 4-7 December 1991*, (World Scientific, Singapore, 1991).
- [11] M.J. Kelly, *Low-Dimensional Semiconductors : Materials, Physics, Technology, Devices*, (Oxford University Press, New York, 1995).
- [12] L.P. Kouwenhoven and C.M. Marcus, “Quantum dots”, *Phys.World*, **11**, 3538 (1998).

- [13] S. Lundquist, G. Morandi, Yu Lu, *Low-Dimensional Quantum Field Theories for Condensed Matter Physicists : Lecture Notes of ICTP Summer Course, Trieste, Italy, September 1992*, (World Scientific, Singapore, 1995).
- [14] A.R. Peaker and H.G. Grimmeiss, *Low-Dimensional Structures in Semiconductors : From Basic Physics to Applications*, (Plenum Press, New York, 1991).
- [15] Fazal Ali, Aditya Gupta, *HEMTs and HBTs : Devices, Fabrication, and Circuits*, (Artech House, Boston, 1991).
- [16] Robert Anholt, *Electrical and Thermal Characterization of MESFETs, HEMTs, and HBTs*, (Artech House, Boston, 1995).
- [17] J. Michael Golio, *Microwave MESFETs and HEMTs*, (Artech House, Boston, 1991).
- [18] K. Brunner, "Si/Ge Nanostructures", Reports on Progress in Phys., **65** (1), 27-72 (2002).
- [19] K. H. Ploog, R. Notzel, "Novel Semiconductor Nanostructures by Functional Self-Organized Epitaxy", Physica E-Low-Dimensional Systems and Nanostructures, **11** (2-3), 78-88 (2001).
- [20] D. Heithmann, V. Gudmundsson, M. Hochgrafe, R. Krahne, D. Pfannkuche, "Far-Infrared Spectroscopy of Tailored Quantum Wires, Quantum Dots and Antidot Arrays", Physica E, **14** (1-2), 37-44 (2002).
- [21] J. P. Connolly, C. Rohr, "Quantum Well Cells for Thermophotovoltaics", Semiconductor Sci. and Techn. **18** (5), 37-44 (2003).
- [22] S. M. Reimann, M. Koskinen, J. Kolehmainen, M. Manninen, D. G. Austing, S. Tarucha, "Electronic and Magnetic Structure of Artificial Atoms", European Phys. Journal D **9** (1-4), 105 (1999).
- [23] D. Goldhaber-Gordon, M.S. Montemerlo, J.C. Love, G.J. Opiteck, and J.C. Ellenbogen, "Overview of Nanoelectronic Devices", Proc. IEEE, **85**, 521540 (1997).
- [24] S. Ciraci, A. Buldum, Inder P. Batra, "Quantum Effects in Electrical and Thermal Transport Through Nanowires", J. Phys.: Condens. Matter, **13**, R537R568 (2001).
- [25] H. Schweizer, M. Jetter, F. Scholz, "Single Quantum Dots: Fundamentals, Applications and New Concepts", Topics in App. Phys. **90**, 185-235 (2003).
- [26] John P. Loehr, *Physics of Strained Quantum Well Lasers*, (Kluwer Academic, Boston, 1998).

- [27] Peter S. Zory, *Quantum Well Lasers*, (Academic Press, Boston, 1993).
- [28] L. Eldada, “Optical Communication Components”, *Review of Scientific Inst.* **75** (3), 575-593 (2004).
- [29] B.J. van Wees, H. van Houten, C.W.J. Beenakker, J.G. Williamson, L.P. Kouwenhoven, D. van der Marel, and C.T. Foxon, “Quantized Conductance of Point Contacts in a Two-Dimensional Electron Gas”, *Phys. Rev. Lett.*, **60**, 848850 (1988).
- [30] H. van Houten and C. Beenakker, “Quantum Point Contacts”, *Phys. Today*, **49** (7), 2227 (1996).
- [31] B. Jeckelmann and B. Jeanneret, “The Quantum Hall Effect as an Electrical Resistance Standard”, *Meas. Sci. Technol.*, **14**, 12291236 (2003).
- [32] Y. Hatsugai, “Topological Aspects of the Quantum Hall effect”, *J. Phys.: Condens. Matter*, **9**, 25072549 (1997).
- [33] T. Chakraborty, P. Pietilainen, *The Fractional Quantum Hall Effect : Properties of an Incompressible Quantum Fluid*, (Springer-Verlag, London, 1988).
- [34] Tapash Chakraborty, Pekka Pietilainen, *The Fractional Quantum Hall Effect : a Survey of the Incompressible Quantum Fluid Including the Integer Quantum Hall Effect* , (Springer-Verlag, New York, 1995).
- [35] Tapash Chakraborty, Pekka Pietilainen, *Quantum Hall Effects : Field Theoretical Approach and Related Topics*, (World Scientific, Singapore, 2000).
- [36] M. Janssen...[et al.];ed.by J. Hajdu, *Introduction to the Theory of the Integer Quantum Hall Effect*, (Weinheim: VCH, 1994).
- [37] Sankar Das Sarma, Aron Pinczuk, *Perspectives in Quantum Hall Effects : Novel Quantum Liquids in Low-Dimensional Semiconductor Structures*, (Wiley, New York, 1997).
- [38] Keshav N. Shrivastava, *Introduction to Quantum Hall Effect*, (Nova Science Publishers, New York, 2002).
- [39] M.Stone, *Quantum Hall Effect*, (World Scientific, Singapore, 1992).
- [40] D. K. Ferry and S. M. Goodnick, *Transport in Nanostructures*, (Cambridge University Press, New York, 1997), p39, p43.
- [41] Gerald Bastard, *Wave Mechanics Applied to Semiconductor Heterostructures*, *Monographies de physique*, p155-191 (1986).

- [42] Gerald Bastard, “Self-Consistent Variational Calculations and Alloy Scattering in Semiconductor Heterojunctions”, *Surface Science* **142**, p284-289 (1984).
- [43] Frank Stern, Sarkar Das Sarma, “Electron Energy Levels in AlGaAs-GaAs Heterojunctions”, *Physical Review B* **30**(2), p840-848 (1984).
- [44] Christopher M. Snowden, *Introduction to Semiconductor Device Modelling*, (World of Scientific Publishing Co Pte Ltd, 1986), p60.
- [45] Strang, G., and G. J. Fix, *An Analysis of the Finite Element Method*, (Prentice-Hall, Englewood Cliffs, 1973).
- [46] Thomas L. Beck, “Real-Space Mesh Techniques in Density-Functional Theory”, *Reviews of Modern Physics*, **72**, 1041 (2000).
- [47] G. E. Kimball and G. H. Shortley, “The Numerical Solution of Schrödinger Equation”, *Phys. Rev.* **45**, 815 (1934).
- [48] L. Pauling, and E. B. Wilson, *Introduction to Quantum Mechanics*, (Dover, New York, 1935), p.202.
- [49] R. Courant, “Variational Methods for the Solution of Problems of Equilibrium and Vibrations”, *Bull. Amer. Math. Soc.*, **49**, pp. 1 (1943).
- [50] I J Schoenberg, “Contributions to the Problem of Approximation of Equidistant Data by Analytic Functions, Part A: On the Problem of Smoothing or Graduation, a First Class of Analytic Approximation Formulas”, *Quart. Appl. Math.*, **4**, 45-99 (1946).
- [51] G. Birkhoff, C. de Boor, B. Swartz and B. Wendroff, “Rayleigh-Ritz Approximation by Piecewise Cubic Polynomials”, *J. Numer. Anal.*, **3**, 188-203 (1966).
- [52] E. L. Albasiny and W. D. Hoskins, “Cubic Spline Solutions to Two-Point Boundary Value Problems” *Comput. J.*, **12**, 151-153 (1969).
- [53] G. D. Byrne and D. N. H. Chi, “Linear Multistep Formulas Based on g-Splines”, *J. Numer. Anal.*, **9**(2), 316-324 (1972).
- [54] B W Shore, “*B*-Spline Expansion Bases for Excited States and Discretized Scattering States”, *J. Chem. Phys.* **63**, 3835-3840 (1975).
- [55] B W Shore, “Solving the Radial Schrödinger Equation by Using Cubic-Spline Basis Functions”, *J. Chem. Phys.*, **58**, 3855 (1973).
- [56] B W Shore, “Use of the Rayleigh-Ritz-Galerkin Method with Cubic Splines for Constructing Single-Particle Bound-State Radial Wavefunctions: The Hydrogen Atom and Its Spectrum”, *J. Phys. B: At. Mol. Phys.*, **6**, 1923-1932 (1973).

- [57] B W Shore, “Comparison of Matrix Methods Applied to the Radial Schrödinger Eigenvalue Equation: The Morse Potential”, *J. Chem. Phys.*, **59**, 6450 (1973).
- [58] B W Shore, “Use of Boundary-Condition Wavefunctions for Bound States, Continuum States, and Resonances”, *J. Phys. B: At. Mol. Phys.*, **7**, 2502-2517 (1974).
- [59] M. Hofmann, M. Bockstedte, and O. Pankratov, “Efficient Self-Consistent Method Using Basis Splines for the Investigation of Interacting Two-Dimensional Electrons in a Random Impurity Potential”, *Phys. Rev. B*, **64**, Art. no. 245321 1-14 (2001).
- [60] J. Sánchez-Dehesa, J. A. Porto, F. Agulló-Rueda, and F. Meseguer, “Electronic Energy Levels of Quantum-Well Wires”, *J. Appl. Phys.*, **73** (10), 5027-5031 (1993).
- [61] J. Sánchez-Dehesa, F. Aristone, and G. E. Marques, “Electronic Levels of Quantum Dots: A Variational Approach”, *J. of the Phys. Soc. Japan*, **69** (12), 3904-3911 (2000).
- [62] J.A. Porto and J. Sánchez-Dehesa, “Theoretical Study of Strained Thin Quantum Wells Grown on Vicinal Surfaces”, *Phys. Rev. B*, **51** (20), 14352-14360 (1995).
- [63] N. Mingo, J.A. Porto and J. Sánchez-Dehesa, “Doping-Profile Effects on the Tunneling Times of Electrons Confined in Double-Barrier Heterostructures”, *Phys. Rev. B*, **50** (16), 11884-11894 (1995).
- [64] C. Goffaux and J. Sánchez-Dehesa, “Two-Dimensional Phononic Crystals Studied Using a Variational Method: Application to Lattices of Locally Resonant Materials” *Phys. Rev. B*, **67**, Art. no. 144301 1-9 (2003).
- [65] Y. Meyer, *Ondelettes, Fonctions Splines et Analyses Graduées*, Lectures given at the University of Torino, Italy (1986).
- [66] Y. Meyer, *Ondelettes et Opérateurs*, Herman, Paris, 1990.
- [67] S. Mallat, “Multiresolution Approximations and Wavelet Orthonormal Bases of $L^2(\mathbf{R})$ ”, *Trans. Amer. Math. Soc.*, **315**, 69-87 (1989).
- [68] C. K. Chui and J. Z. Wang, J. Joannopoulos, and P. K. Lam, “A cardinal Spline Approach to Wavelets”, *Proc. Amer. Math. Soc.*, **113**, 785-793 (1991).
- [69] K. Cho, T. A. Arias, J. Joannopoulos, and P. K. Lam, “Wavelets in Electronic Structure Calculations”, *Phys. Rev. Lett.*, **71**, 1808-1811 (1993).
- [70] T. A. Arias, “Multiresolution Analysis of Electronic Structure: Semicardinal and Wavelet Bases”, *Rev. Mod. Phys.*, **71**, 267 (1999).

- [71] A. B. Fowler, F. F. Fang, W. E. Howard, and P. J. Stiles, “Magneto-Oscillatory Conductance in Silicon Surfaces”, *Phys. Rev. Lett.*, **16**, 901-903 (1966).
- [72] H. L. Störmer, A. C. Gossard, and W. Wiegmann, “Observation of Intersubband Scattering in a 2-Dimensional Electron System”, *Solid State Commun.* **41**, 707-709 (1982).
- [73] L. Pfeiffer, K. W. West, H. L. Störmer, and K. W. Baldwin, “Electron Mobilities Exceeding 10^7 cm²/V s in Modulation-Doped GaAs”, *Appl. Phys. Lett.* **55**, 1888-1890 (1989).
- [74] F. Stern and S. Das Sarma, “Electron Energy Levels in GaAs-Ga_{1-x}Al_xAs Heterojunctions”, *Phys. Rev. B.* **30**, 840-848 (1984).
- [75] E. Buks, M. Heiblum, Y. Levinson, and H. Shtrikman, “Scattering of a Two-Dimensional Electron Gas by a Correlated System of Ionized Donors”, *Semicond. Sci. Technol.* **9**, 2031 (1994).
- [76] K. Hirakawa and H. Sakaki, “Mobility of the Two-Dimensional Electron Gas at Selectively Doped n-Type Al_xGa_{1-x}As/GaAs Heterojunctions with Controlled Electron Concentrations”, *Phys. Rev. B.* **33**, 8291-8303 (1986).
- [77] R. Schuster, K. Ensslin, D. Wharam, S. Kühn, J. P. Kotthaus, G. Böhm, W. Klein, G. Tränkle, and G. Weimann, “Phase-Coherent Electrons in a Finite Antidot Lattice”, *Phys. Rev. B.* **49**, 8510-8513 (1994).
- [78] D. Weiss, K. v. Klitzing, K. Ploog, and G. Weimann, “Magnetoresistance Oscillations in a Two-Dimensional Electron Gas Induced by a Submicrometer Periodic Potential”, *Europhys. Lett.* **8**(2), 179-184 (1989).
- [79] A. K. Geim, R. Taboryski, A. Kristensen, S. V. Dubonos, and P. E. Lindelof, “High-Field Magnetoresistance in a Periodically Modulated Two-Dimensional Electron Gas”, *Phys. Rev. B.* **46**, 4324-4327 (1992).
- [80] J. P. Kotthaus and D. Heitmann, “On the Realizability of Artificial Superlattices in Inversion Layer Systems”, *Surf. Science* **113**, 481-484 (1982).
- [81] Altan M. Ferendeci, *Solid State and Electron Devices*, (McGraw-Hill, Singapore, 1991) .
- [82] Ersan Demiralp and Haluk Beker, “Properties of Bound States of the Schrödinger equation with Attractive Dirac Delta Potentials”, *J. Phys. A: Math. Gen.* **36**, 74497459 (2003).
- [83] H. J. Korsch and S. Mossmann, “Stark Resonances for a Double δ Quantum Well: Crossing Scenarios, Exceptional Points and Geometric Phases”, *J. Phys. A: Math. Gen.* **36**, 21392153 (2003).

- [84] M. I. Molina and C. A. Bustamante, “The Attractive Nonlinear Delta-Function Potential”, *Am. J. Phys.* **70** (1), 67-70 (2002).
- [85] Jason P. Modisette, Peter Nordlander, James L. Kinsey, Bruce R. Johnson, “Wavelet Bases in Eigenvalue Problems in Quantum Mechanics”, *Chemical Physics Letters* **250**, 485-494 (1996).
- [86] H. Bachau, E. Cormier, P. Decleva, J. E. Hansen and F. Martin, “Applications of *B*-Splines in Atomic and Molecular physics”, *Rep. Prog. Phys.*, **64**, 1815-1942 (2001).
- [87] I. Daubechies, *Ten Lectures on Wavelets*, SIAM, Philadelphia, 1992.
- [88] E. Hernández and G. Weiss, *A First Course on Wavelets*, CRC Press, 1996.
- [89] Paul L. DeVries, *A First Course in Computational Physics*, (Willey & Sons 1994), p254.
- [90] J. R. Alvarez-Collado and Robert J. Buenker, “On the Numerical Solution of the Multidimensional Vibrational Time-Independent Schroedinger Equation”, *J. Comp. Chem.*, **13**(2), 135-141 (1992).

VITA

Bora Dikmen was born in Eskişehir on October 13, 1969. He got married to Miss Elçin Emir, and has a lovely daughter.

He received his B.S. degree from Department of Electrical Engineering (EE) of the Middle East Technical University (METU) in Ankara, in 1991. He got his Master of Science degree in Physics from METU Physics Department in 1996. He was a research assistant between 1991 and 1999 at the same department.

His research has mainly concentrated on the computational physics of low-dimensional structures, under the guidance of Prof. Mehmet Tomak from the METU Physics Department. During some parts of his research in this field, he collaborated with Prof. Kemal Leblebicioğlu from METU EE Department.

The results of his research is scheduled to appear in International Journal of Modern Physics C (IJMPC) 16; issue 2 (2005).